

TOPICAL REVIEW

Molecular imaging using recolliding electrons

Manfred LeinInstitut für Physik and Center for Interdisciplinary Nanostructure Science and Technology,
Universität Kassel, Heinrich-Plett-Straße 40, 34132 Kassel, Germany

Received 24 November 2005, in final form 19 June 2007

Published 3 August 2007

Online at stacks.iop.org/JPhysB/40/R135**Abstract**

When molecules are subject to intense laser pulses, electrons can be detached, accelerated and driven back to the molecule, resulting in electron–ion recollisions. Recolliding electrons probe the structure and dynamics of molecules. We review the theoretical concepts and experimental achievements towards using recollisions to image molecules. We classify these methods by the choice of the observed signal, which can be one of high-harmonic radiation, electrons from high-order above-threshold ionization, or fragment kinetic energies from recollision-induced dissociation or Coulomb explosion. It is shown that sub-Ångström and sub-femtosecond resolution is possible within these schemes.

(Some figures in this article are in colour only in the electronic version)

1. Introduction

Investigating the structure of matter and observing its time evolution is one of the fundamental tasks in physics and chemistry. Measurements with high spatial and temporal resolution have always been a major challenge. Recent breakthroughs in this direction were the tomographic imaging of an electron wavefunction in molecular nitrogen [1] and the fastest ever measurement of proton dynamics in H_2^+ [2]. Both works fall into the domain of this review and will be described in detail in section 5.

Phenomena in the realm of atomic and molecular physics are typically associated with length and time scales that are many orders of magnitude smaller than those of our daily life. Typical time scales are picoseconds for molecular rotation, femtoseconds for vibration and attoseconds for electronic dynamics. Typical length scales are below 1 nm for small molecules. It is well known that the structure of matter on the atomic scale is well accessible by methods such as x-ray or electron diffraction [3–5]. Today these techniques are not necessarily restricted to the solid state: for example, molecular reactions in the gas phase could be traced by electron diffraction with picosecond resolution [5]. Nevertheless, these methods have difficulties to resolve the typical timescale of 100 fs for ultrafast motion of atoms inside small molecules. A milestone in the development of ultrafast methods has been the pump-probe spectroscopy

based on short laser pulses [6]. Using femtosecond pulses, the evolution of a chemical reaction could be traced for the first time. Today femtosecond spectroscopy is well established, and one of the current efforts is to push the pump-probe method into the domain of sub-femtosecond phenomena, and consequently being able to watch the motion of electrons on their natural attosecond time scale [7].

The conventional pump-probe schemes can tell us about the speed of phenomena, and they have even led to quantum control techniques that allow us to steer processes into a desired direction by using appropriately shaped pulses [8, 9]. However, in contrast to a technique such as diffraction, these schemes have difficulties to give direct information on structure. This means that although they give access to time scales, there may be remaining uncertainties about the precise nature of the rearrangement in the system of interest.

We conclude that novel methods combining structure determination with femtosecond or even sub-femtosecond time resolution are highly desirable. In this topical review, we discuss the emerging field of ultrafast molecular imaging using *recolliding electron wave packets*. Electrons created by ionization in a strong laser field can be accelerated and driven back to the core since the electric field in a laser pulse is alternating. In the electron–core recollision, the instantaneous state of the molecule is probed by the electron wave packet in a way similar to conventional electron diffraction. In principle, every possible product of the electron recollision can be an observable in such a scheme. We will discuss the following scenarios:

- Elastic electron scattering (see the work on atoms in [10]). In this case we detect the electron. The scheme is analogous to conventional electron diffraction with an external electron beam [5], but the electron flux is much higher in the recollision scheme [11].
- Inelastic scattering causing further ionization or excitation of the core, thereby initiating fragmentation [11]. Here the fragment kinetic-energy release is the observable to measure. Inelastic scattering is familiar from double ionization of atoms [12–15] and molecules [16–20].
- Recombination accompanied by the emission of a photon. This process is known as high-order harmonic generation (HHG) [21, 22]. HHG can be utilized for the generation of attosecond pulse trains [23–25] and isolated attosecond pulses [26, 27] in laser–atom interactions. It is therefore fundamental to the field of attosecond science [28–30].

For each of the three cases, we will describe how to extract information about the molecular structure from the observables and discuss the experimental progress.

Concerning the time resolution, we first note that the shortest duration of a strong optical laser pulse that can be made in the laboratory today is a few femtoseconds [31–33]. This sets the time resolution for the methods described above when they are used within a pump-probe scheme, where, for example, a pump laser pulse starts a chemical reaction and the probe pulse performs the recollision imaging step. In addition to this, we will review approaches where sub-femtosecond time resolution has been achieved by placing the pump and probe processes not in two separate laser pulses, but rather within a single pulse [2, 11]. In this case, the ionization of the molecule by the laser field at a certain instant represents the pump process, while the recollision of the electron wave packet represents the probe process. As we will see, the delay between these two steps can be controlled or selected with a resolution of less than a femtosecond. It is then possible to combine sub-femtosecond time resolution with sub-Ångström spatial resolution.

Molecular imaging based on electron recollisions is an emerging research area, where a number of methods have been proposed and demonstrated. It is clear that the accuracy of imaging depends to a large extent on the control of the recolliding electron wave packet.

The ideal wave packet would be such that the electron wavelength is much smaller than the molecule to be imaged, while the wave front should be flat over the dimension of the molecule. Furthermore, the duration of the recollision that is responsible for the measured signal should be as short as possible to allow for the imaging of ultrafast dynamics. Although these requirements are only partially met by the present-day laser pulses, there is no doubt that the further development of laser sources will open up the possibility for precise control so that imaging will become a very accurate technique. Infrared laser pulses as they are now generated, e.g. at the advanced laser light source in Canada [34], represent progress in this direction. Proposals to control recollision wave packets are the subject of current research [35].

The imaging methods can be divided into two types: (a) methods exploiting the wave nature of the recolliding electron in order to have a diffraction-like process, (b) methods based on recollision-induced dissociation or Coulomb explosion, where the structural information is found in the fragment kinetic energies. We note that Coulomb explosion induced directly by laser ionization (without rescattering) is an established technique: some of the latest works pushing the time resolution down to a few femtoseconds are found in [36–38].

It is interesting to compare the recollision methods with conventional electron diffraction. The latter is a very clean technique in the sense that the electron energy can be easily controlled, but it is difficult to apply to dynamics of molecules in the gas phase because the probability that an electron hits a target molecule is very small. In contrast, under the influence of a strong laser pulse, a substantial portion of the molecules can be ionized and therefore the probability for electron collision is limited only by the spreading of the electron wave packet. Moreover, femtosecond or even sub-femtosecond time resolution is rather straightforward to achieve in the recollision method. The difficulty lies more in the distinction of the diffracted electrons from direct photoelectrons and in accounting for the influence of the laser field on the final electron energies.

Laser alignment of molecules plays an important role in many of the imaging experiments. Clearly, an aligned ensemble allows much more detailed measurements than randomly oriented molecules. We will not discuss this topic in detail, but only mention the two basic techniques, adiabatic alignment [39–42] with relatively long (e.g., picosecond) pulses and nonadiabatic alignment [43, 44] with relatively short femtosecond pulses. The latter has the advantage that it creates laser-field-free aligned ensembles at the revival times of the rotational dynamics. [45] presents a direct theoretical comparison. Using pulse trains to achieve high degrees of alignment is suggested in [46]. A comprehensive review about molecular alignment is found in [47].

This topical review is organized as follows. We first discuss the physics of molecules in strong femtosecond laser pulses, where we focus in particular on the three-step recollision mechanism and physical phenomena related to it. We then describe the three different areas of recollision imaging in ‘historical’ order (according to when they were proposed): (i) electron diffraction, (ii) the fragmentation method and (iii) the HHG-based approach. The first topic represents the shortest part since there is only theoretical work published up to now. The third topic seems to attract the fastest growing interest at present and fills the most sizable section of this review. It includes the two examples mentioned in the beginning.

2. Molecules in strong laser fields

2.1. Ionization dynamics

In this review, we discuss the interaction of molecules with laser pulses that are strong enough to induce significant ionization and are beyond the realm of perturbation theory. This is the case

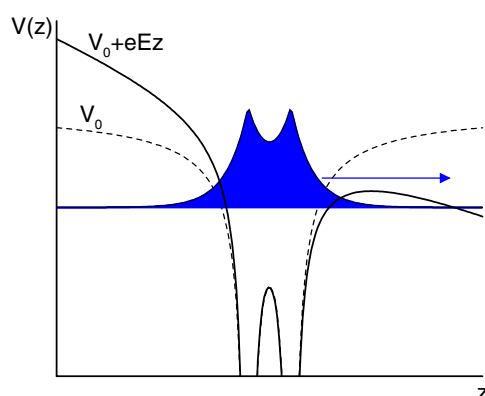


Figure 1. Schematic picture of tunnelling ionization in a diatomic molecule under the influence of the instantaneous electric field strength E (directed along the negative z -axis in this example).

for femtosecond laser pulses in the visible or infrared regime, which are routinely produced in laser laboratories today. On the other hand, for the purpose of imaging, the laser intensity should be moderate, in order not to destroy the molecules already during the rising edge of the pulses. We restrict ourselves to the non-relativistic regime for the electron dynamics, and we will always assume the dipole approximation. This means that the laser–molecule interaction is theoretically described by the time-dependent Schrödinger equation where the magnetic field of the laser pulse is neglected. The laser acts merely via the electric field, which is—as seen from the viewpoint of the molecule—time dependent but homogeneous in space. Except for the section on inelastic rescattering, we will restrict ourselves to the case that only one electron becomes active at a time, i.e., if one electron is set free in an ionization event, all other electrons will stay bound in their ground state.

One usually makes a distinction of intense-laser–matter interaction into the multiphoton regime (low intensity/high frequency) and tunnelling regime (high intensity/low frequency), while for very high field strengths neither of the two pictures is applicable because one enters the over-barrier regime where the binding potential is distorted so much that an electron can escape classically from the system into the continuum [48].

Most of the imaging proposals rest on the basic assumption that the interaction between molecule and laser field is approximately quasistatic, i.e. it is meaningful to describe the interaction in terms of an instantaneous electric field. The description in terms of multiphoton absorption, although valid, will not be as useful to understand the physical phenomena.

At time t during the action of a laser pulse, the field-free binding potential V_0 that a valence electron sees is distorted by the presence of the instantaneous electric field $\mathbf{E}(t)$. The total potential is

$$V(\mathbf{r}) = V_0(\mathbf{r}) + e\mathbf{E}(t) \cdot \mathbf{r}, \quad (1)$$

where \mathbf{r} and $-e$ are position and charge of the electron. In the quasistatic picture, the change of the electric field is slow enough for the bound electron to react instantaneously, i.e. the bound-state wavefunction adjusts to the distorted potential and most importantly, the electron has time to tunnel through the potential barrier into the exterior so that the molecule is ionized. The tunnelling process is shown schematically in figure 1. Once an electron has escaped from the core region, it is strongly accelerated by the laser field with little influence from the binding potential. Since the electric field oscillates, the electron will follow some type of oscillatory motion.

In the following, a few aspects of the electron dynamics are derived from a classical picture: in the simplest possible approximation, the electron dynamics is treated classically with the initial conditions that the electron starts with zero velocity at position zero at time $t = t_0$. The resulting model is also known as the simple man's model. Newton's equation for this situation is

$$m\dot{\mathbf{r}} = -e\mathbf{E}(t). \quad (2)$$

In order to have a significant probability for recollision, we require in the following that the laser field is linearly polarized,

$$\mathbf{E}(t) = E(t)\mathbf{e}_z, \quad (3)$$

since in this case, the electron is accelerated along a straight line, while in the case of elliptical or circular polarization, the electron follows a curved trajectory and will normally miss the core. Many important features of the electron dynamics can be studied with the example of a monochromatic electric field $E(t) = E_0 \sin(\omega t)$. In this case, the solution of equation (2) with the initial conditions stated above is

$$z(t) = \alpha \sin(\omega t) - \alpha \sin(\omega t_0) - \alpha\omega(t - t_0) \cos(\omega t_0), \quad (4)$$

$$x(t) = y(t) = 0, \quad (5)$$

with the classical oscillation amplitude

$$\alpha = \frac{eE_0}{m\omega^2}. \quad (6)$$

The corresponding electron velocity in the polarization direction is

$$\dot{z}(t) = \alpha\omega \cos(\omega t) - \alpha\omega \cos(\omega t_0), \quad (7)$$

meaning that the electron has a drift velocity $v_D = -\alpha\omega \cos(\omega t_0)$ superposed by an oscillating term with amplitude $\alpha\omega = eE_0/(m\omega)$. We see that the magnitude and direction of the drift velocity depend on the time of ionization, t_0 . From this, one can for instance calculate the maximum momentum of the emitted photoelectron: if the laser pulse is not too short, the oscillations die out adiabatically, i.e. the final velocity equals the drift velocity. The maximum velocity is therefore $v_{\max} = \alpha\omega$, and consequently the maximum kinetic energy is $mv_{\max}^2/2 = e^2E_0^2/(2m\omega^2)$. This holds for the so-called direct electrons, which do not rescatter from the core, but go directly to the detector. During the action of the laser field, the instantaneous kinetic energy is

$$E_{\text{kin}}(t) = \frac{m}{2}\alpha^2\omega^2[\cos^2(\omega t) - 2\cos(\omega t)\cos(\omega t_0) + \cos^2(\omega t_0)], \quad (8)$$

so the average kinetic energy over an optical cycle of the laser field is

$$\bar{E}_{\text{kin}} = U_p[1 + 2\cos^2(\omega t_0)], \quad (9)$$

where

$$U_p = \frac{e^2E_0^2}{4m\omega^2} \quad (10)$$

is the *ponderomotive potential*. Its interpretation is the average kinetic energy related to the oscillatory electron motion. The kinetic energy related to the drift motion is given by the other contribution in equation (9),

$$E_{\text{drift}} = 2U_p \cos^2(\omega t_0). \quad (11)$$

From the last equation, it is once more apparent that the maximum energy of direct electrons is $2U_p$. Since the electron energy is typically larger than the energy of those electrons that absorb only the minimum number of photons needed for ionization, one speaks about ‘above-threshold ionization’ (ATI).

The derivation presented here assumes a monochromatic field. Although the results are useful down to surprisingly short laser pulse durations, it is clear that modifications are necessary for few-cycle pulses. A review on ionization in few-cycle pulses can be found in [49].

2.2. Electron recollision

In view of molecular imaging, we are predominantly interested in the possibility that the electron returns to the core in order to take a ‘snapshot’ of the molecule. The time of return, t_1 , is determined by the nonalgebraic equation $z(t_1) = 0$, where $z(t)$ is given by equation (4) for a monochromatic field. For given starting time t_0 , there may be zero, one or more solutions for t_1 . We refer to the difference $\tau = t_1 - t_0$ as the travel time of the electron. An important quantity is the return energy E_r of the electron which has been shown to have the maximum value of $E_{r,\max} \approx 3.17U_p$ in the pioneering work by Corkum [50]. In HHG, the emitted photon energy equals return energy plus binding energy of the electron in the ground state. This means that the cutoff in the HHG spectrum is at the photon energy $3.17U_p + I_p$, where I_p is the ionization potential of the molecule. Quantum mechanical corrections lead to the slightly modified cutoff $3.17U_p + 1.32I_p$ [51].

A given return energy can be realized by not only one but at least two different electron trajectories, the short and long trajectories (or ‘orbits’). Most HHG experimental setups are such that—taking advantage of the phase-matching conditions for the generation of harmonics in a focussed beam—only the short trajectories contribute significantly to the HHG spectrum [28, 52–54]. The predictions of the classical model for the short trajectories can be cast into a useful fit formula relating the return energy to the travel time,

$$\omega\tau = 0.786[f(E_r/U_p)]^{1.207} + 3.304[f(E_r/U_p)]^{0.492}, \quad (12)$$

where $f(x) = \arccos(1 - x/1.5866)/\pi$. The fact that different return energies correspond to different return times t_1 makes the harmonic frequency dependent upon the emission time, i.e. the harmonic radiation is *chirped* on a sub-femtosecond time scale. If we ignore the long trajectories, there is a one-to-one correspondence between return energy and travel time. This will be exploited in a scheme to measure nuclear dynamics (to be discussed in section 5). Figure 2 shows the return energy as a function of $\omega\tau$. The red part of the curve ($\omega\tau = 0 \dots 4.09$) represents the short trajectories.

In reality, the electron is not born with exactly zero momentum in the continuum. Rather, there is a distribution of initial momenta, giving rise to the spreading of the electron wave packet after ionization. This suppresses the efficiency of recollision. However, it serves a useful purpose as far as imaging is concerned, since it guarantees, at least for few-atom molecules, that the returning wave packet will sweep over the entire molecule rather than covering only part of the molecule. Thus, a snapshot of the whole molecule can be taken. To give an example, for H_2 in a 40 fs 800 nm pulse having an intensity of $1.5 \times 10^{14} \text{ W cm}^{-2}$, the diameter of the returning electron wave packet has been estimated to be about 15 Å from measured ellipticity dependences of fragment yields [11, 30].

One of the proposals towards molecular imaging is based on electron diffraction in elastic rescattering, i.e. the electron scatters once before going to the detector. For this case, the extension of the classical model is such that at the time of recollision, the electron is

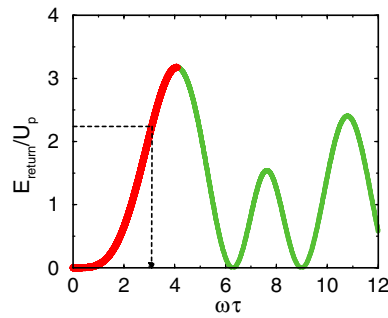


Figure 2. Kinetic energy of recolliding electrons in the classical model as a function of $\omega\tau$ where τ is the travel time of the electron.

deflected by a certain angle, but with unchanged absolute value of the velocity. It can be shown numerically that the maximum final kinetic energy of the rescattering electrons is approximately $10U_p$ [55, 56]. This maximum value is realized in the case of scattering by 180° . Ionization via rescattering is thus responsible for high-order ATI.

For simplicity, we have ignored the effect of the Coulomb potential on the continuum electron. This could in principle be taken into account in the equation of motion. Coulomb focusing [57] of the electron wave packet is an important consequence of the Coulomb force: it strongly enhances the current density of the returning electron.

2.3. Symmetry considerations

Although the classical recollision model usually works well for atoms and molecules, special situations exist where a modification must be made in the initial conditions. Most importantly, in the case of a laser field applied to orbitals with mirror antisymmetry such that the field is parallel to the nodal plane, the initial velocity of the electron cannot be chosen to be zero. This is because the momentum-space distribution of the orbital has zero probability for electrons with a zero momentum component perpendicular to the nodal plane. This symmetry property is not broken by the field, if it is parallel to the nodal plane, and therefore no electrons can recollide strictly on the axis. The recollision probability will thus be very small. In this particular case, elliptical polarization can enhance the recollision probability [16, 58] by compensating the lateral electron drift. Another possibility has been proposed in [59], where it was shown in a non-dipole calculation that for sufficiently high laser intensity, the force due to the magnetic field of the laser pulse can partially compensate the lateral drift. Experiments and theory on aligned CO_2 [60], which possesses a π_g highest occupied molecular orbital (HOMO) with two nodal planes, confirmed that HHG is suppressed for alignment parallel to the laser field, as expected for this type of orbital symmetry. Similar conclusions were drawn from calculations [61–63] and experiments [64] comparing aligned N_2 and O_2 , showing that HHG from O_2 is maximized for orientations around 45° with respect to the laser field while for N_2 , parallel alignment is preferential. The shape of the π_g HOMO of O_2 is very similar to that of CO_2 . The HOMO of N_2 , by contrast, has σ_g symmetry and is therefore mirror symmetric to planes along the molecular axis and perpendicular to it. The influence of symmetry was seen also in the calculated ellipticity dependences of HHG from symmetric and antisymmetric orbitals [65]. Recently, measurements of HHG from aligned organic molecules with π_u -type orbitals have been reported for the first time [66], showing again the typical signature of orbital symmetry.

We note that the antisymmetry leads also to strong suppression of the total ionization probability when the electric field points along a nodal plane. Lagmago Kamta and Bandrauk have shown that the initial electron orbital can be qualitatively imaged from the orientation dependence of the ionization probability of ground and excited states of H_2^+ in strong laser pulses [67].

2.4. Theoretical treatment

Beyond the simple man's model, the theoretical treatment of molecules in strong laser fields usually follows one of three approaches:

- (i) numerical solution of the time-dependent Schrödinger equation (TDSE), $i\hbar(\partial/\partial t)\Psi = H\Psi$,
- (ii) strong-field approximation (SFA) or related methods,
- (iii) Floquet-type calculations.

One should note that the TDSE approach is normally restricted to model systems, since already the dynamics of two electrons in a strong laser pulse is too demanding for present-day computers unless the system (molecule plus field) possesses cylindrical symmetry as in the case of the He atom [68, 69]. Therefore it is popular to employ the single-active-electron approximation (SAE) and/or reduced dimensionality of the molecular system of interest. The SFA [51, 70–72] is a partially analytical method that we will describe in more detail later in the context of HHG. It has the advantage of much shorter computational times. Therefore, although the SFA is usually formulated within the SAE approximation, too, it has the practical advantage that one can easily do many runs with varying parameters. Moreover, the SFA gives some degree of analytical understanding and is therefore more amenable to physical interpretation than TDSE results. The Floquet approach [73, 74] is particularly useful for strictly periodic fields and becomes more involved for short laser pulses.

We finally mention the molecular Ammosov–Delone–Krainov (MO-ADK) tunnelling theory [75] as another approach. This theory, however, covers only the ionization step and must be combined with additional ingredients to describe the three-step scenario [76, 77].

2.5. Remarks on molecular size

Before discussing in detail the recollision imaging methods, we point out that we are mainly concerned with small molecules near their equilibrium geometry, i.e. with internuclear distances of the order of atomic units. One of our basic assumptions is therefore that the recollision wave packet has a diameter much larger than the molecule, as stated above. For very large molecules or for diatomic molecules stretched to large distances, the physical situation is entirely different because an electron may tunnel out from one site and collide with a different site. The collision energies can significantly exceed the atomic value of $3.17U_p$. For HHG, a cutoff up to $8U_p + I_p$ is predicted [78–81], or even higher if additional elastic scattering events are taken into account [82]. This pathway to HHG might be difficult to observe since it requires the electron wavefunction to be coherently delocalized over the two sites [83]. This restriction does not apply to the analogous effect predicted for ATI. Elastic scattering of a tunnelled electron from a different site leads to electron energies up to $18U_p$ [84], or higher if multiple scattering is taken into account. Since the cutoff depends on the internuclear distance, it may be possible to exploit the effect for imaging of large molecules. Due to the low efficiency of scattering, however, the ultrahigh-energy cutoff has not been experimentally demonstrated yet.

3. Electron diffraction

We define the term ‘diffraction’ as follows: an incident wave is scattered from an object in a way such that interference between different pathways takes place, resulting in an interference pattern in the scattered wave. For example, the interference between the sound waves from two speakers is not included in this definition. In the present context, diffraction imaging then stands for observing the interference pattern due to scattering of laser-driven recolliding electrons from the molecular core.

The principle of diffraction imaging of a molecule with its own electron was initially suggested by Zuo *et al* in [85]. It represents the first proposal towards recollision imaging. Note, however, that the numerical results of the paper [85] focussed on few-photon absorption and did not reflect the diffraction of rescattering electrons. Rather they showed the interference of the direct electron waves coming from the two centres of H_2^+ at internuclear distances of 20 au and 30 au, when subject to an intense laser pulse. The observed angular distributions exhibit the signature of two-centre interference in direct ionization and thus reflect the molecular structure in much the same way as was later discussed by Faisal and coworkers for the systems N_2 and O_2 [86] and also seen experimentally [87].

The physics of rescattering in atomic above-threshold ionization (ATI) has been discussed in detail by Paulus and coworkers. They explained the presence of high-energy electrons in the ATI spectra of atoms by the rescattering process and derived the cutoff at $10U_p$ from a classical analysis [10, 55, 56].

Among the recollision imaging methods, diffraction is the one in closest analogy to conventional imaging and it is expected to give the most direct information about the molecule: in principle the experiment on a fixed-in-space molecule would yield an electron angular distribution that has encoded in it the molecular structure. However, the efficiency of the elastic scattering process is very small. As a consequence, if one measures electrons with relatively low energy, where the yield is easily measurable, one is overrun by the direct ATI electrons. On the other hand, if one measures high-energy electrons, which can originate only from rescattering, the signal is extremely small. Nevertheless, some indications of diffraction have been seen in unpublished measurements by the group of Corkum [88].

3.1. Simulations of diffraction

The theory of electron diffraction in ATI was investigated in 2D TDSE calculations and in a semiclassical analysis in [89]. More detailed work was carried out later in [90], and 3D TDSE results followed in [91, 92].

In the 2D simulations [89, 90], one solves the TDSE, which in the velocity-gauge form for linearly polarized light reads

$$i\hbar \frac{\partial \Psi(\mathbf{r}, t)}{\partial t} = \left(\frac{\mathbf{p}^2}{2m} + \frac{p_z}{m} eA(t) + V(\mathbf{r}) \right) \Psi(\mathbf{r}, t), \quad (13)$$

with $A(t) = -\int_{-\infty}^t E(t') dt'$. Care needs to be taken to retain the information about outgoing electrons in order to calculate ATI spectra. If the numerical grid cannot be made large enough to capture the entire electron wavefunction, a splitting technique [89, 93–95] is needed where the electron wavefunction outside the grid is stored in the form of a plane-wave expansion.

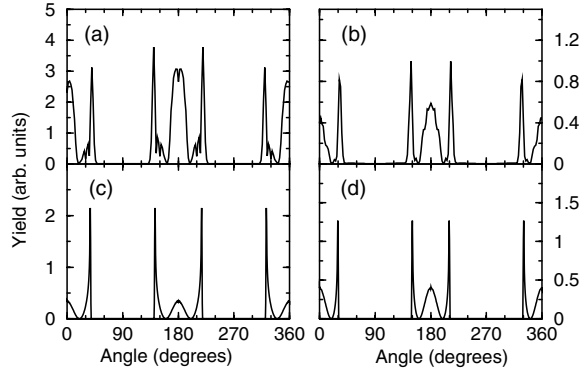


Figure 3. Angular distributions of ATI electrons from 2D H_2^+ at $R = 2$ au aligned perpendicular to the polarization axis of a 780 nm pulse with intensity $5 \times 10^{14} \text{ W cm}^{-2}$. (a) and (b) show results from numerical solution of TDSE for electron energies $7U_p$ and $8U_p$. (c) and (d) are the predictions of the semiclassical model. The electric field of the laser pulse is trapezoidally shaped with 3-cycle linear ramps and 10 cycles total duration. From [89]. Copyright (2002) by the American Physical Society.

In the reduced dimensional TDSE, it is common to use a soft-core Coulomb potential. For H_2^+ , we use

$$V(\mathbf{r}) = -e^2 \sum_{k=1,2} \frac{1}{\sqrt{(\mathbf{r} - \mathbf{r}_k)^2 + 0.5}}, \quad (14)$$

where \mathbf{r}_1 and \mathbf{r}_2 are the positions of the two nuclei, and the internuclear distance is $R = 2$ au. Two examples of electron angular distributions from H_2^+ aligned perpendicular to the electric field of the applied laser pulse are shown in figures 3(a) and (b). To understand the results, we compare the numerical results with a semiclassical model based on classical trajectories, but including the phase difference between the trajectories scattered from two different centres. The model builds on the classical electron dynamics after ionization at time t_0 , as outlined in the previous section. If the electron is elastically scattered by an angle ϑ_0 within the yz -plane at the time of return, t_1 , the final velocity of the electron is given by

$$\dot{z}_f = \alpha\omega \{ \cos \vartheta_0 [\cos(\omega t_1) - \cos(\omega t_0)] - \cos(\omega t_1) \}, \quad (15)$$

$$\dot{y}_f = \alpha\omega \sin \vartheta_0 [\cos(\omega t_1) - \cos(\omega t_0)], \quad (16)$$

where the shift by $-\alpha\omega \cos(\omega t_1)$ in equation (15) is due to the acceleration of the electron in the laser field after scattering. To be consistent with the 2D TDSE calculation, we assume that the scattered electron moves within the plane spanned by the electric field and molecular axis. The two centres give rise to two scattered waves with a phase difference. The phase difference has two contributions: (i) a phase difference φ_1 from the different distances that the incident electron has to travel *before* reaching the two nuclei,

$$\varphi_1 = \frac{m}{\hbar} \dot{z}_{\text{return}} R \cos \theta, \quad (17)$$

where θ is orientation of the molecule (angle between electric field and molecular axis); (ii) a phase difference φ_2 from the different distances in the trajectories *after* scattering,

$$\varphi_2 = -\frac{m}{\hbar} \dot{z}_{\text{return}} R (\cos \vartheta_0 \cos \theta + \sin \vartheta_0 \sin \theta). \quad (18)$$

In the case of perpendicular alignment ($\theta = 90$ degrees), we have

$$\varphi_1 = 0, \quad (19)$$

$$\varphi_2 = -\frac{m}{\hbar} \dot{z}_{\text{return}} R \sin \vartheta_0 = -\frac{m}{\hbar} \dot{y}_{\text{f}} R. \quad (20)$$

A correction should be made when one deals with long-ranged potentials such as (14): the recolliding electron is accelerated significantly by the binding potential before it scatters from the core. We can take this effect approximately into account by an *ad hoc* modification of the phase difference. Assuming that the electron kinetic energy E_{kin} is increased by the binding potential I_{p} means that the recollision velocity is increased by a factor

$$\beta = \sqrt{(E_{\text{kin}} + I_{\text{p}})/E_{\text{kin}}}. \quad (21)$$

We therefore assume that the total phase difference is $\varphi = \beta(\varphi_1 + \varphi_2)$. A related heuristic correction is the subject of discussion in the next section in the context of HHG.

Figures 3(c), (d) show the results of the semiclassical model for the simplified assumption of uniform distributions of ionization times and scattering angles. Both methods of calculation yield the same main feature of the angular distribution, namely a strong modulation, with zeros that originate from destructive interference. The electron energies $7U_{\text{p}}$ and $8U_{\text{p}}$ are chosen such that only rescattered electrons contribute to the angular distribution. These results are a clear proof of the existence of electron diffraction in a quantum mechanical calculation with realistic laser parameters.

A systematic and thorough investigation of the interference signatures was presented by Spanner *et al* [90]. They identified the complexities that make the ATI electron spectrum difficult to read as follows:

- (i) *The imprint of the initial state of the molecule on the recolliding wave packet.* For example, as noted before, for antisymmetric orbitals placed with the nodal plane along the electric field, no electrons are emitted strictly along the field.
- (ii) *Holographic-type structures.* For low electron energies, direct and scattered electron waves with the same final energy may be superposed, giving rise to holographic interference. This may be avoided by concentrating on high-energy electrons, or one may think of exploiting the effect in order to extract information about the molecule, similar to conventional holography.
- (iii) *Large scattering angles.* Fast ATI electrons are separated most clearly from the direct electrons, but their production requires large scattering angles in the rescattering step. The quickly decreasing cross section is responsible for a small signal and for a distorted diffraction image.
- (iv) *Acceleration of the electrons by the laser field after rescattering.* This is apparent in equation (15). The final momenta are therefore not directly useful for determining whether the interference is constructive or destructive. Instead of the usual angular distribution for fixed final energy, the more natural distribution that should be considered is a distribution for fixed recollision energy, see below.
- (v) *Interference between electron waves with different recollision energies.* A given final electron velocity vector may be realized by different electron trajectories with different recollision energies. In this case the diffraction image may be difficult to interpret.

Spanner *et al* [90] demonstrated the most natural way to extract the diffraction information from the final momentum distribution: as in a conventional diffraction setup, one is interested in the angular distribution of electrons with fixed energy of incidence, i.e. fixed recollision energy. Immediately after rescattering, these electrons are found on a spherical surface (circle in 2D) with its centre at the origin in momentum space. Afterwards, the electron is accelerated

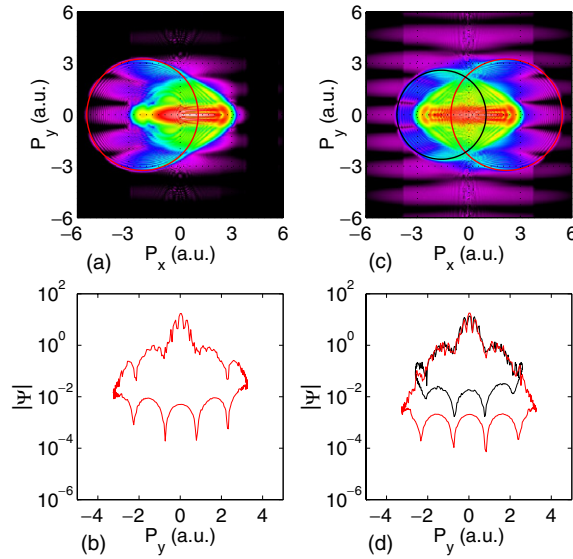


Figure 4. ATI electron momentum distributions for 2D H_2^+ at $R = 4$ au aligned perpendicular to the polarization axis of an 800 nm pulse with intensity $I \approx 6.9 \times 10^{14} \text{ W cm}^{-2}$. (a) 1.25 cycle pulse with constant amplitude; (b) \cos^2 -shaped 5 fs pulse. (c) and (d) show diffraction patterns along circular cuts as described in the text. Reprinted with permission from [90].

by the laser field, so in the final momentum distribution, the sphere/circle is displaced by an amount which is determined by the time of recollision, t_1 . From equation (15) we see that the shift equals $-\alpha\omega \cos(\omega t_1)$ for a monochromatic field $E(t) = E_0 \sin(\omega t)$. Plotted in figure 4 are the final momentum distributions of ATI electrons for 2D H_2^+ at $R = 4$ au subject to 800 nm ultrashort laser pulses with intensity $I \approx 6.9 \times 10^{14} \text{ W cm}^{-2}$ and two different pulse shapes. Circular cuts corresponding to trajectories with different ionization time are indicated. The value along these circles is plotted in the lower panels. One can see clearly that this isolates the diffraction images for the corresponding recollision energies. The structures in the strong peak around zero momentum are due to the holographic interferences. The interference between short and long trajectories leading to the same final velocity is responsible for the ring-like structures in the momentum distribution. We see that these interferences do not destroy the diffraction image that is obtained by taking the circular cut.

3.2. Extracting molecular structure

It remains to be discussed how the internuclear distance of a diatomic molecule can be extracted from a diffraction image. This question has been addressed in [91, 92], where fully three-dimensional TDSE calculations have been carried out. In [92], a Fourier method analogous to conventional electron diffraction was successfully applied to the TDSE results for a K_2^+ molecule at $R = 7.6$ au (and other internuclear distances) subject to an 800 nm laser field. However, the TDSE results of [92] are not explainable by an intuitive double-slit picture since the first-order diffraction spots are not found along the direction of the molecular axis but in the perpendicular direction (i.e., the direction not included in the 2D models described above).

The TDSE results by Yurchenko *et al* [91] for H_2^+ at $R = 6$ au subject to a 400 nm laser field do show interference spots along the direction of the molecular axis as expected intuitively. The upper panels of figure 5 show the 3D electron density distributions for two

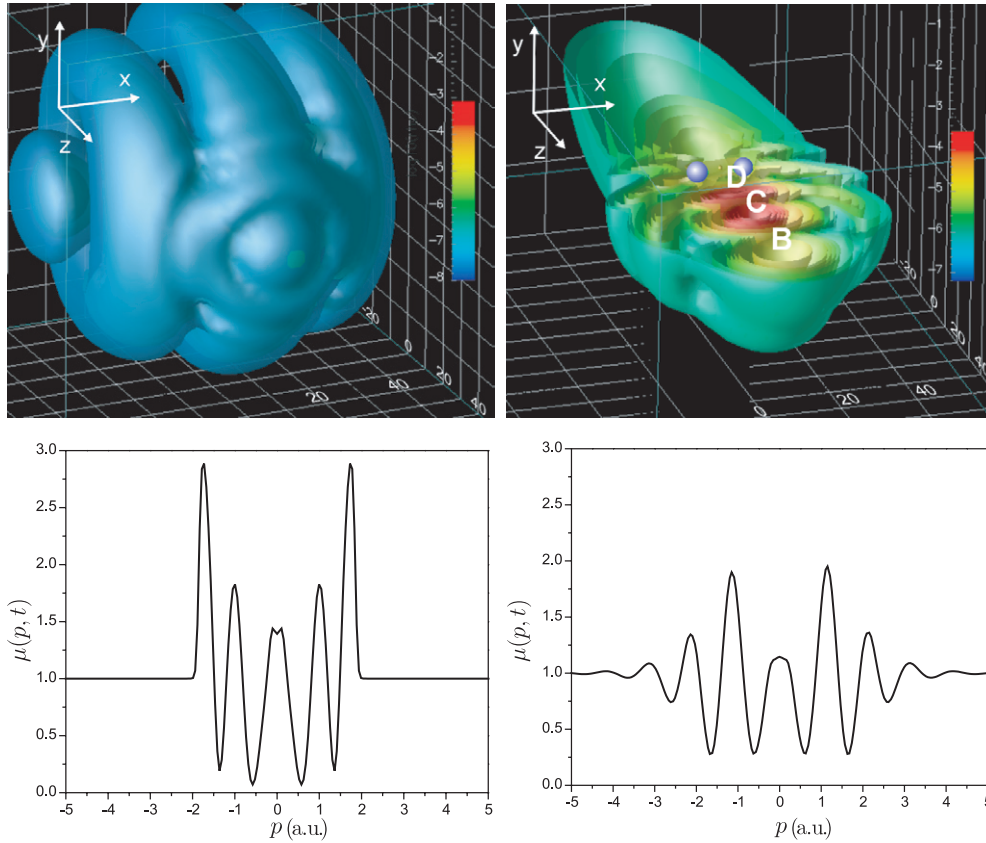


Figure 5. Upper panels: electron density distributions for the diffraction of a Gaussian wave packet (upper left) and laser-induced diffraction (upper right) in $3D H_2^+$ at $R = 6$ au. Lower panels: momentum-distribution ratios μ as described in the text for the Gaussian wave packet (lower left) and for the laser pulse (lower right). Reprinted with permission from [91]. Copyright (2004) by the American Physical Society.

cases: (i) diffraction of a Gaussian wave packet in the absence of a laser field (upper left panel) and (ii) laser-induced diffraction in a single-cycle pulse of intensity $3 \times 10^{14} \text{ W cm}^{-2}$ polarized along the z -axis (upper right panel). The initial momentum of the Gaussian wave packet was chosen such that it matches the maximum recollision momentum in the laser pulse. Note that the electron wave packet moves along the z -axis, and the molecular axis points along the x -axis. Therefore the modulation of the density as a function of x is the signature of diffraction.

In order to isolate the diffraction image from the momentum distribution, the authors of [91] use an elegant trick: they use the momentum distribution perpendicular to the molecular axis (i.e., in the y -direction) as a reference. The ratio $\mu(p)$ of the parallel and the perpendicular distributions,

$$\mu(p) = \frac{\int |\Psi(p, p_y, p_z)|^2 dp_y dp_z}{\int |\Psi(p_x, p, p_z)|^2 dp_x dp_z} \quad (22)$$

exhibits a clear diffraction pattern, which no longer suffers from the problem that the momentum distributions always show a rapid falloff with increasing momentum. This ratio μ is shown in figure 5 for the Gaussian wave packet (lower left panel) and the laser-induced

case (lower right panel). Although the peaks have different heights, both curves show very similar oscillating behaviour.

To extract the internuclear distance, the authors of [91] took advantage of the geometry with the molecular axis aligned perpendicular to the electric field of the laser pulse. In this case, the interference condition is simplified as explained above, and the spacing between the diffraction peaks in the momentum distribution along the molecular axis is a direct measure of the internuclear distance (see equation (20)), if one neglects the Coulomb correction factor β , equation (21).

Although diffraction appears to be the most natural way to exploit recollisions towards molecular imaging, experimentally there has not been a full demonstration so far in contrast to the methods to be described in the following sections. This is obviously a consequence of the complexities listed above. The question how to read the diffraction image is largely answered, but severe problems remain such as the low yield of high-energy rescattered electrons.

4. Fragmentation

The basic principle of the fragmentation method is closely related to Coulomb explosion imaging [96, 97], where a molecule is doubly ionized so that fragmentation into two positively charged ions takes place under a strongly repulsive Coulomb interaction, leading to fast fragments. The kinetic-energy release can be directly related to the starting inter-ion distance if the two fragments have zero initial kinetic energy. The normal situation in Coulomb explosion imaging is that a laser pulse is responsible for the second ionization step and thus triggers the explosion. (The first ionization step may have been achieved, for example, within the same pulse or by a separate laser pulse.) In the recollision-based method, the returning electron serves as the trigger that starts the fragmentation, by exciting or ionizing the molecular core. In contrast to electron diffraction, we now deal with *inelastic* scattering of the recolliding electron.

What is the reason to study the recollision-induced fragmentation rather than the more direct process, where fragmentation is initiated by laser-induced ionization? The recolliding electron wave packet has the appealing feature of *sub-laser-cycle duration*. A measurement of the recollision channel therefore offers the possibility of sub-cycle time resolution. This was first suggested by Niikura *et al* in [11] for the fragmentation of H_2 in strong laser pulses. The control of the recollision time in this scheme, however, is not easy and was achieved by variation of the laser wavelength in the follow-up work [98]. Interestingly, the high-energy recollision channel in the proton kinetic-energy spectrum, which is the essential observable in this scheme, had not been observed much earlier than the work by Niikura *et al*. It is first mentioned by Staudte *et al* [17] who, at the time, were not certain about the origin of the high-energy feature. Later, the process was investigated in detail by the same group [99, 100], coming to the conclusion that recollision-induced excitation to an excited bound state of H_2^+ , followed by laser-induced ionization is the mechanism responsible for the production of the high-energy protons in their experiment. We note that recollision excitation followed by field ionization is known to play an important role in atomic double ionization [101, 102]; recent discussions of this process in H_2 can be found in [19, 20].

The method is able to measure sub-laser-cycle dynamics because of the presence of correlated wave packets: ionization launches simultaneously an electron wave packet in the continuum and a nuclear wave packet in the Born–Oppenheimer (BO) potential of the molecular ion. In the simplest modelling, the initial nuclear wave packet is the same as the vibrational ground state of the neutral molecule (Franck–Condon principle). Deviations due to the dependence of the ionization rate on the internuclear distance have been reported by Urbain

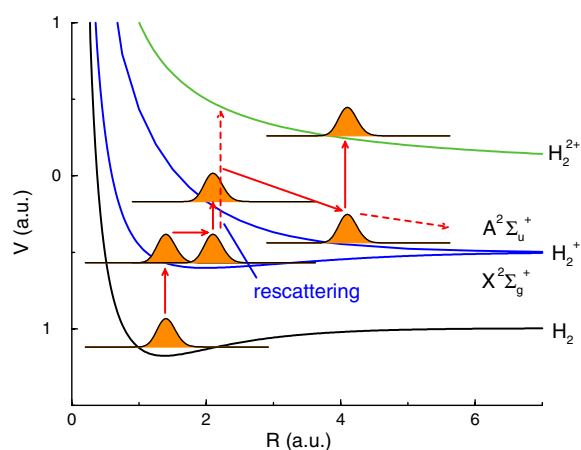


Figure 6. Born–Oppenheimer potentials of H_2 (electronic ground state), H_2^+ (ground and first excited state), and two bare protons (H_2^{2+}). The pathways to laser-induced fragmentation are indicated. The solid red arrows show the dominant pathway in the ‘molecular clock’ according to [99, 100]. Dashed lines indicate other pathways to fragmentation.

et al [103]. After ionization, one of the wave packets can serve as a clock to measure the evolution of the other wave packet. The scheme is therefore often referred to as a ‘molecular clock’.

4.1. Pathways to fragmentation

We start with an explanation of the various pathways to fragmentation in hydrogen molecules subject to strong laser pulses. The relevant BO potentials of H_2 and H_2^+ are shown in figure 6. Initially, the molecule is in the vibrational ground state of the electronic ground-state BO potential. Since the laser field does not couple directly to the vibrational degree of freedom, and since the laser frequency is not resonant with any low-lying excitation, the preferential response of the molecule will be tunnel ionization. This creates a nuclear wave packet in the electronic ground state of H_2^+ . After ionization, the internuclear distance initially increases in the course of the wave-packet evolution. At the same time, the high initial vertical ionization potential and the energy gap to the first excited state decrease so that further ionization/excitation becomes more favourable. Three possibilities have been discussed in [100, 104]: (i) *rescattering excitation* (as proposed in [11]) with the chance of subsequent ionization from the excited state; (ii) *sequential ionization* [104, 105], i.e. ionization by the laser field alone, at a time when the instantaneous electric field reaches a peak value; (iii) *enhanced ionization* when the molecular ion reaches the critical internuclear distance of ~ 5 au. Enhanced ionization [106, 107] stands for the enormous increase of the ionization rate at certain internuclear distances where the electron is dynamically localized at one nucleus and finds the tunnelling barrier suppressed by the presence of the other nucleus. We note that enhanced ionization can be viewed as a subclass of sequential ionization since in both cases two electrons are removed independently without the need for electron–electron correlation [19]. Yet, some authors reserve the expression ‘sequential’ for removal of the second electron before the molecule reaches the critical distance for enhanced ionization.

Each of the three processes populates a repulsive BO curve at an internuclear distance characteristic of the type of process, leading to a distinct final fragment energy. The kinetic-energy spectrum for double ionization thus shows three peaks, see the measurement by Alnaser

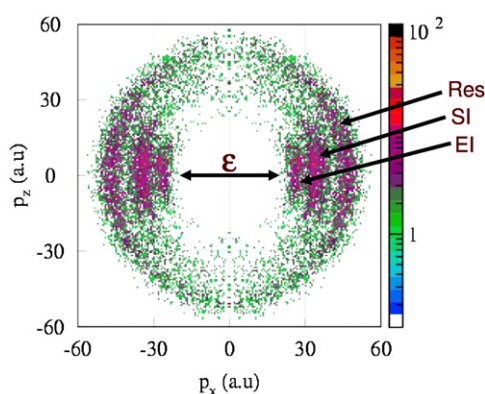


Figure 7. Experimental momentum image of proton pairs from fragmentation of H_2 in 14 fs laser pulses of $3 \times 10^{14} \text{ W cm}^{-2}$ intensity. The rescattering (Res), sequential ionization (SI) and enhanced ionization (EI) channels are indicated by arrows. Reprinted with permission from [100]. Copyright (2004) by the American Physical Society.

et al [100] shown in figure 7. The rescattering process occurs largely within one or two optical cycles after ionization and gives rise to the highest energy. For significant sequential ionization, a strong electric field, i.e. peak value, combined with low enough ionization potential, i.e. stretched molecule, is needed. It therefore happens at a later time, producing less energetic fragments. Enhanced ionization takes place at the large critical distance and thus yields even slower fragments. Note that the term ‘dissociation’ is not normally used for the fragmentation into two ions.

We focus here on the rescattering channel. Within a semiclassical calculation, Niikura *et al* analysed carefully the time structure of the recolliding electron wave packets. They followed many electron trajectories in the field of the laser and the residual ion, with initial conditions that follow from tunnelling ionization theory [108] combined with their measurement of the ellipticity dependence of the signal [11]. They counted the returning electrons passing through an area of the size of the $\Sigma_g \rightarrow \Sigma_u$ excitation cross section of H_2^+ , considering only electrons with energies sufficient for this transition. The resulting electron current density as a function of time is shown in figure 8. It is noticeable that (i) the current density reaches huge values, and (ii) the first return has by far the largest weight.

There is a controversial discussion about the question whether the observed ions from the rescattering pathway come mainly from dissociation into $H+H^+$ or rather from subsequent further ionization and Coulomb explosion into H^++H^+ . The first alternative was assumed in the original work by Niikura *et al* [11, 98] and seems to be confirmed by recent time-dependent wave-packet simulations [109, 110], although the approximations made in the latter works have been questioned [111]. On the other hand, the presence of the two-ion channel is proven by the coincidence measurements of Alnaser *et al* [99, 100], see figure 7, and by the calculations of Tong *et al* [76, 77]. Incidentally, the quantitative predictions of both models (with and without second ionization) for the fragment kinetic energies are very similar.

4.2. The molecular clock

We discuss first the measurement by Niikura *et al*. They investigated D_2 molecules in laser pulses of four different wavelengths, 800 nm, 1200 nm, 1530 nm and 1850 nm. In order to avoid laser coupling between the lowest electronic states in D_2^+ they restricted the

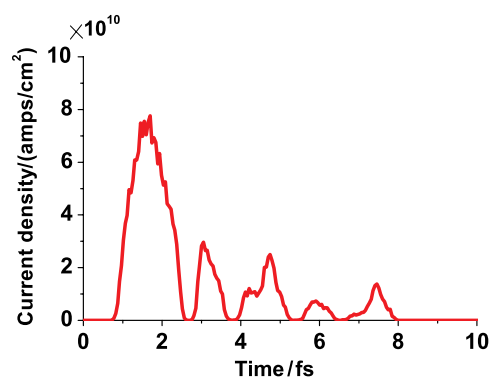


Figure 8. Calculated electron current density experienced by the H_2^+ ion for an 800 nm laser pulse with intensity $1.5 \times 10^{14} \text{ W cm}^{-2}$. Reprinted with permission from [11]. Copyright (2002) by the Nature Publishing Group.

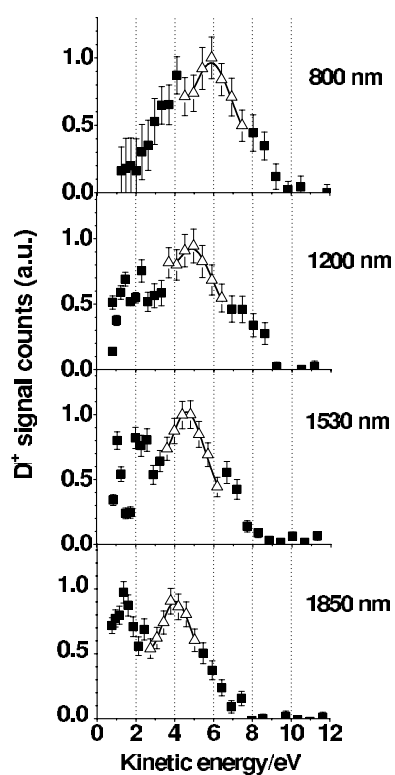


Figure 9. Measured deuteron kinetic-energy spectra resulting from D_2 in 40 fs laser pulses with intensity $1.5 \times 10^{14} \text{ W cm}^{-2}$ and wavelengths as indicated. Different wavelengths correspond to different recollision times. Reprinted with permission from [98]. Copyright (2003) by the Nature Publishing Group.

measurement to molecules aligned perpendicular to the laser polarization, by counting only the fragments emitted in this direction. This suppresses the enhanced ionization peak. The energy distributions of the deuterons are shown in figure 9. The open data points indicate the channel for which the energy is consistent with the interpretation in terms of dissociation on

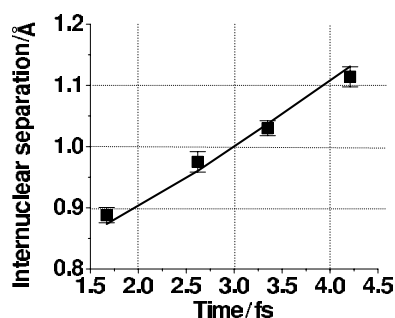


Figure 10. Vibrational wave-packet position as a function of time, as reconstructed from the data in figure 9. It is assumed that the deuterons stem from dissociation into $D+D^+$. Reprinted with permission from [98]. Copyright (2003) by the Nature Publishing Group.

the Σ_u state, induced by inelastic rescattering during the first return of the electron. Longer laser wavelengths correspond to later recollision times and therefore to larger values of the internuclear distance and lower kinetic energy. Using the reflection principle [112], the vibrational wave packet at the time of recollision can be retrieved from the energy distribution. To complete the analysis, one needs to determine the recollision time from the laser wavelength. Using the arrival time of the first electron bunch (see figure 8), one arrives at the reconstructed time evolution of the internuclear distance (wave-packet position) as shown in figure 10. It agrees well with the result of a numerical wave-packet propagation on the Σ_g ground state of D_2^+ (solid line in figure 10). This is a measurement of molecular dynamics with a time resolution of about 1 fs.

Alnaser *et al* [99] disentangled the dissociation and the double-ionization channel by measuring the coincident and noncoincident emitted deuterons for 800 nm laser pulses. Already at intensities between 1×10^{14} and 2×10^{14} W cm $^{-2}$, they find that about half of all detected deuterons come from double ionization. Tong *et al* [76, 77] have carried out a detailed theoretical analysis of the complete process. They used their MO-ADK ionization theory [75] for the neutral molecule and the molecular ion. The electron follows classical trajectories in the combined field of the laser pulse and the ion [113, 114] with initial conditions based on tunnelling theory. Cross sections for the electron impact excitation of the molecular ion are not directly available, but have been deduced by Tong *et al* from tabulated values for atomic cross sections. They emphasize the importance of including not only transitions to the Σ_u state but also transitions to the higher excited Π_u state of the ion. The resulting kinetic-energy spectrum for 800 nm laser pulses with the same pulse length and intensity as used in the experiment of [98] is shown in figure 11(a). Note that the energy scale used by Tong *et al* refers to the total kinetic-energy release, i.e. the energy of both fragments, rather than the kinetic energy of individual D^+ ions as in Niikura *et al*'s work. The calculated spectrum agrees well with the experiment, see figure 9. However, the calculation shows that at least for 800 nm, the contribution of dissociation to the total yield is small (dashed line in figure 11(a)). Moreover, from the separation into the contributions from rescattering events in different optical cycles, figure 11(b), we find that the highest peak in the total spectrum is due to rescattering during the second cycle after ionization, which could mean either the second or third return of the electron, cf figure 8. A detailed analysis shows that the peak is in fact due to rescattering at the third return of the electron.

The calculated results for the various laser wavelengths of the experiment show the shift of the peaks towards lower energy with increasing wavelength, see figure 12(a). This is a

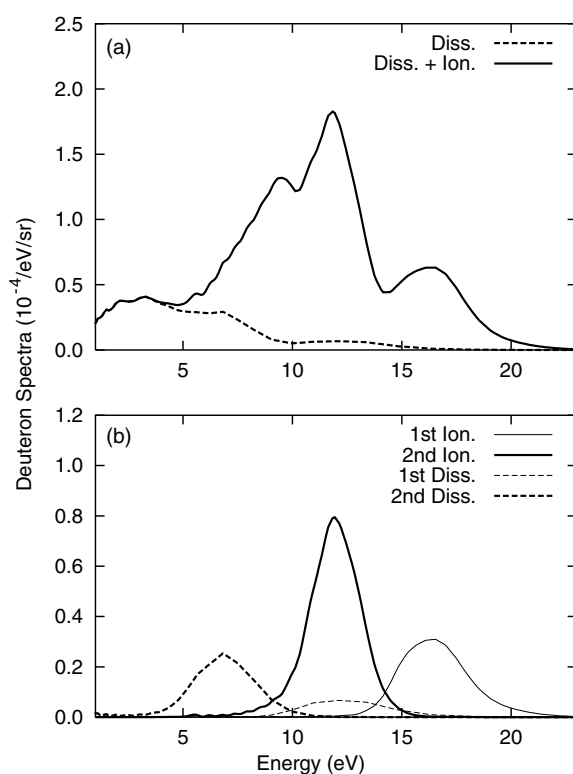


Figure 11. (a) Total kinetic-energy release for fragmentation of D₂ in 800 nm laser pulses with intensity $1.5 \times 10^{14} \text{ W cm}^{-2}$ and pulse length 40 fs, calculated within the rescattering model. Dashed line, contribution from dissociation alone. (b) Spectrum analysed into contributions from double ionization and dissociation due to rescattering in the first or second optical cycle after ionization, as indicated. Reprinted with permission from [76]. Copyright (2003) by the American Physical Society.

clear indication that the molecular clock works despite the modified interpretation. Larger wavelength implies a longer delay time between ionization and rescattering and therefore a larger internuclear distance at the time of rescattering, leading to a lower final kinetic energy. However, both the times and distances measured by the molecular clock according to the modified model by Tong *et al* are significantly larger since the model attributes the main peak of the spectra to the third rather than the first return, cf table 1 of [76]. Finally, panel (b) of figure 12 shows the influence of the pulse length on the molecular clock. Clearly, the peaks are sharper for shorter pulses, i.e. the measurement of the energy (and therefore internuclear distance) is more accurate. This is due to the suppression of later returns in the shorter pulse.

The coincidence measurements by Alnaser *et al* [99] confirm that a significant portion of the D⁺ ions is from double ionization rather than dissociation. However, the dissociation channel for rescattering at the first electron return gives rise to a peak at almost the same energy as double ionization for rescattering at the third return, see the peaks at 12 eV in figure 11(b). This means that in principle both channels can be valid assumptions for analysing the data. A coincidence measurement is necessary for an unambiguous measurement of the recollision time and internuclear distance. If one concentrates on the double-ionization channel, the different return times appear to be well separated from each other. The left side of figure 13 displays the measured spectra for double ionization of H₂ using different laser pulses [100].

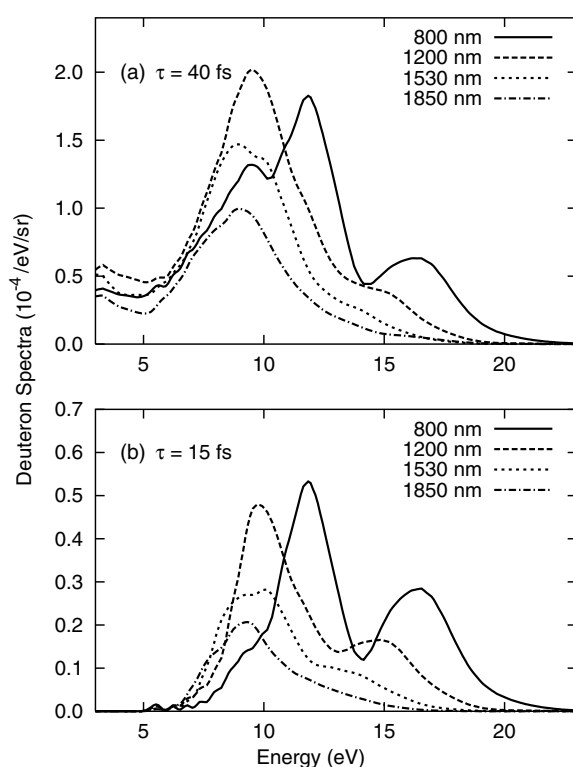


Figure 12. (a) Total kinetic-energy release for laser pulses as in figure 11 but with various different laser wavelengths. (b) Same as (a) for the shorter pulse length 15 fs. Reprinted with permission from [76]. Copyright (2003) by the American Physical Society.

The right-hand side shows the results of the rescattering model as described above, where the contributions from the first and third return have been separated out. An important conclusion from these data is that in sufficiently short pulses (8 fs in the lower panel of figure 13), the later returns as well as the enhanced-ionization peak are suppressed so that the first recollision dominates the spectrum. Concerning the accuracy of the molecular clock, a disadvantage of the double-ionization channel is the uncertainty about the precise time of the second ionization step.

We conclude that the molecular clock offers the possibility of probing molecular dynamics with sub-cycle temporal resolution and sub-Ångström spatial resolution. However, it requires precise knowledge of the fragmentation mechanism in order to read the clock correctly. Ideally, this requires few-cycle pulses and coincidence measurements of the fragments.

5. High-harmonic generation

This section contains three parts: (i) a brief introduction to the strong-field approximation for HHG, also known as the Lewenstein model [51], as it is the basis of several imaging proposals, (ii) methods for imaging of static molecular structure and (iii) dynamical imaging with a discussion of nuclear-motion effects on harmonic spectra.

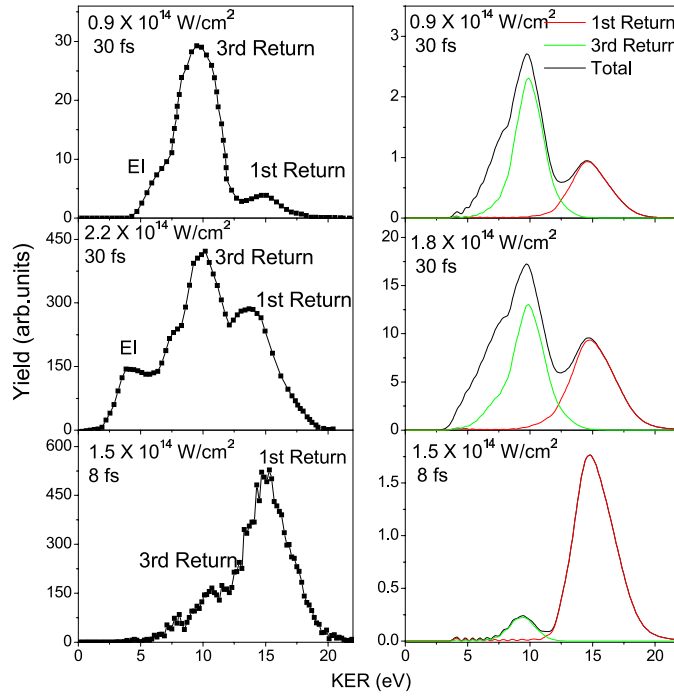


Figure 13. Comparison of kinetic-energy-release spectra for H_2 in 790 nm pulses with different intensities and pulse lengths. Left: experiment, right: rescattering model. Reprinted with permission from [100]. Copyright (2004) by the American Physical Society.

5.1. The strong-field approximation

The time-dependent Hamiltonian in dipole approximation for a one-electron system driven by the electric field $E(t)$ of a linearly polarized laser pulse reads

$$H = \frac{\mathbf{p}^2}{2m} + V(\mathbf{r}) + eE(t)z. \quad (23)$$

The harmonic spectrum $S(\omega)$, i.e. the spectrum of the emitted coherent radiation, is proportional to the power spectrum of the dipole acceleration [115–118]. The spectrum $S_e(\omega)$ of harmonics polarized along direction e is

$$S_e(\omega) \sim |e \cdot \mathbf{a}(\omega)|^2, \quad (24)$$

where ω is the harmonic frequency and $\mathbf{a}(\omega)$ is the temporal Fourier transform of the time-dependent dipole acceleration

$$\mathbf{a}(t) = \ddot{\mathbf{D}}(t), \quad (25)$$

with $\mathbf{D}(t) = \langle -e\mathbf{r} \rangle$ being the time-dependent expectation value of the dipole moment. The strong-field approximation for the time-dependent electron wavefunction means that (i) the electron is unaffected by the laser field until the time t' of ionization and (ii) afterwards the electron moves in the laser field only, unaffected by the binding potential. Furthermore, we neglect the depletion of the bound state as is often done. This leads to the dipole moment (without terms corresponding to continuum–continuum transitions) [51]

$$\mathbf{D}(t) = -\frac{i}{\hbar} \int_0^t dt' \int d^3p d_t^* (\mathbf{p} + e\mathbf{A}(t)) d_i (\mathbf{p} + e\mathbf{A}(t'), t') \exp[-iS(\mathbf{p}, t, t')/\hbar] + \text{c.c.} \quad (26)$$

where $S(\mathbf{p}, t, t') = \int_{t'}^t dt'' [(\mathbf{p} + e\mathbf{A}(t''))^2 / (2m) + I_p]$ is the semiclassical action with the ionization potential I_p , $\mathbf{A}(t) = -\int_{-\infty}^t \mathbf{E}(t') dt'$, and the ionization and recombination matrix elements are given by

$$d_i(\mathbf{p}, t) = \langle \psi_{\text{PW}}(\mathbf{p}) | eE(t)z | \psi_0 \rangle, \quad (27)$$

$$d_r(\mathbf{p}) = \langle \psi_{\text{PW}}(\mathbf{p}) | -e\mathbf{r} | \psi_0 \rangle \quad (28)$$

with plane-wave states $\psi_{\text{PW}}(\mathbf{p})$ of momentum \mathbf{p} , normalized in the momentum scale. The appearance of plane waves is the essential point of the SFA. It facilitates easy computation but is the main source of errors at the same time. In practice, saddle-point approximations are additionally applied to the integral in equation (26) [51, 81].

Instead of evaluating the dipole moment, equation (26), followed by the double time derivative, equation (25), one may alternatively evaluate directly the acceleration expectation value via the Ehrenfest theorem [117, 119], or evaluate the momentum expectation value followed by a single time derivative [120]. Although the dipole formulation above has been the most widely used version, we note that the *momentum form* appears to be the most reliable version of the Lewenstein model for molecules [120].

5.2. Imaging molecular structure

The first indication that HHG spectra from molecules carry information about the molecular structure came from early simulations for H_2^+ [80, 121, 122] and H_2 [121], and from the first HHG experiments with adiabatically aligned [39–42] molecules (CS_2 , CO_2), showing that HHG depends on the orientation of the molecular axis [60, 123, 124]. Initially the main goal of such experiments was to search for optimal conditions for HHG, in order to improve coherent XUV light emission. Later, HHG started to become used towards the investigation of molecular structure. This development was triggered by a series of calculations on the orientation dependence of HHG in H_2^+ and H_2 [125–130], providing growing evidence for interference effects analogous to electron diffraction: a double-slit-type interference pattern is present in harmonic spectra from the simplest diatomic molecules H_2^+ and H_2 . The direct experimental confirmation of the intramolecular two-centre interference effect was first achieved for aligned CO_2 [131, 132]. These works make use of the nonadiabatic molecular alignment technique [43, 44] to control alignment in combination with HHG [64]. Itatani *et al* went a major step forward towards molecular-orbital imaging: they performed a complete tomographic reconstruction of the electron orbital in N_2 from the spectra measured at various orientations of the molecular axis [1]. A series of studies then investigated the theoretical basis of the orbital tomography method, addressing questions such as the multielectron nature of the initial electronic molecular state [133–136].

The first demonstration of two-centre interference was given within the 2D H_2^+ model with fixed nuclei where the potential is given by equation (14). When harmonic spectra are calculated from the numerical solution of the TDSE, the method of choice is to evaluate the time-dependent dipole acceleration $\mathbf{a}(t)$ via the Ehrenfest theorem [117],

$$m\mathbf{a}(t) = e\langle \Psi(t) | \nabla V + e\mathbf{E}(t) | \Psi(t) \rangle. \quad (29)$$

Then the harmonic spectrum follows from equation (24). The resulting spectra for 2D H_2^+ , aligned at various different angles with respect to the polarization axis of a linearly polarized 780 nm laser pulse, are shown in figure 14. Two different laser intensities are compared. Furthermore, panel (d) of the figure shows the result of a laser-field-free simulation where the initial state is the superposition of the ground state with an incoming electron wave packet,

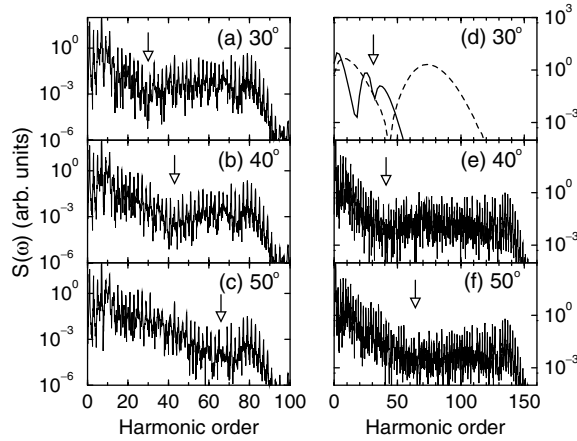


Figure 14. Spectra of harmonics polarized parallel to the laser polarization direction for 2D H_2^+ in 780 nm laser pulses, aligned at various angles as indicated. Left panels: laser pulses with intensity $5 \times 10^{14} \text{ W cm}^{-2}$. Panel (d): field-free simulation for recolliding wave packets with energies corresponding to the 31st harmonic (solid line) and 75th harmonic (dashed line). Panels (e), (f): laser pulses with intensity $1 \times 10^{15} \text{ W cm}^{-2}$. From [125]. Copyright (2002) by the American Physical Society.

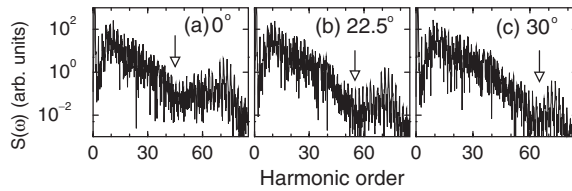


Figure 15. Spectra of harmonics polarized parallel to the laser polarization direction for 2D H_2 in 780 nm laser pulses with intensity $5 \times 10^{14} \text{ W cm}^{-2}$. The molecule is aligned at various angles as indicated. From [125]. Copyright (2002) by the American Physical Society.

the momentum of which is chosen such that it corresponds to the 31st or 75th harmonic, respectively. In all cases, we observe a clear suppression of harmonic emission around a harmonic frequency that depends on the orientation angle but is independent of the laser parameters. The same observation can be made in the results of time-dependent Hartree–Fock calculations for the case of 2D H_2 . In addition to the potential given by equation (14) with softening parameter 0.41 instead of 0.5, the H_2 model assumes a mean-field potential

$$V_{\text{ee}}(\mathbf{r}) = e^2 \int \frac{|\Psi(\mathbf{r}', t)|^2 d^2 r'}{\sqrt{(\mathbf{r} - \mathbf{r}')^2 + 0.36}} \quad (30)$$

describing the electron–electron interaction. The results for various orientations of this model molecule are shown in figure 15. Similar to H_2^+ , the HHG spectra exhibit a minimum moving to higher harmonic orders with increasing angle between molecule and laser field.

In view of using HHG for attosecond pulse generation, a very interesting quantity is the harmonic phase, which can be calculated simply as the phase of the complex Fourier transformed acceleration, $a(\omega)$. Figure 16 compares the orientation dependences of the harmonic intensity and of the harmonic phase for the 43rd harmonic in 2D H_2^+ . It is apparent that the minimum in the harmonic yield coincides with a jump of the phase about π , while

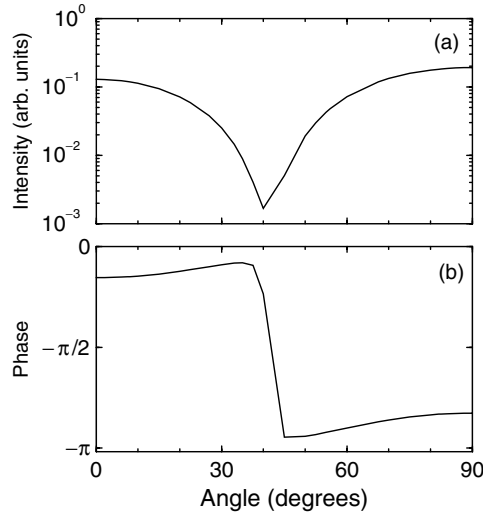


Figure 16. Orientation dependence of the 43rd harmonic for 2D H_2^+ in a 780 nm laser pulse with intensity $5 \times 10^{14} \text{ W cm}^{-2}$. (a) Harmonic intensity. (b) Harmonic phase. From [126]. Copyright (2002) by the American Physical Society.

the phase is roughly constant otherwise. This suggests that the complex harmonic amplitude $a(\omega)$ goes through zero at a certain angle of orientation.

In order to corroborate the idea of two-centre interference, data from extensive simulations for H_2^+ and H_2 were collected [126], and the positions of the minima found in the spectra and in the orientation dependences were compared with a simple double-slit formula. If the contributions from the two centres interfere with a phase difference determined by the de Broglie wavelength λ of the returning electron and the projection of the internuclear distance on the laser polarization axis, $R \cos \theta$, then interference minima are expected for

$$R \cos \theta = (2n + 1) \frac{\lambda}{2}, \quad n = 0, 1, 2, \dots, \quad (31)$$

while interference maxima are expected for

$$R \cos \theta = n\lambda, \quad n = 1, 2, \dots \quad (32)$$

The result of the comparison is plotted in figure 17. The straight lines show the predictions of the simple formulae (31), (32), also known as the two-point emitter model. The minima and maxima found from the numerical TDSE calculations are plotted as data points. It is important to note here, that a heuristically corrected relation between electron wavelength $\lambda = 2\pi/k$ and harmonic frequency ω is used to make this plot,

$$\frac{\hbar^2 k^2}{2m} = \hbar\omega, \quad (33)$$

instead of the usual relation $\hbar^2 k^2 / (2m) + I_p = \hbar\omega$ that emerges from the SFA or simple man's model. The idea behind this correction is that the interference is not determined by the wavelength corresponding to the asymptotic energy of the electron far away from the core, $E_{\text{asympt}} = \hbar\omega - I_p$. The interference depends rather on the wavelength in the core region, where the electron is faster due to the attractive long-range binding potential. The energy amount I_p appears to be the natural scale of such a correction. We then observe in figure 17 that the numerical results agree well with the two-point emitter model using

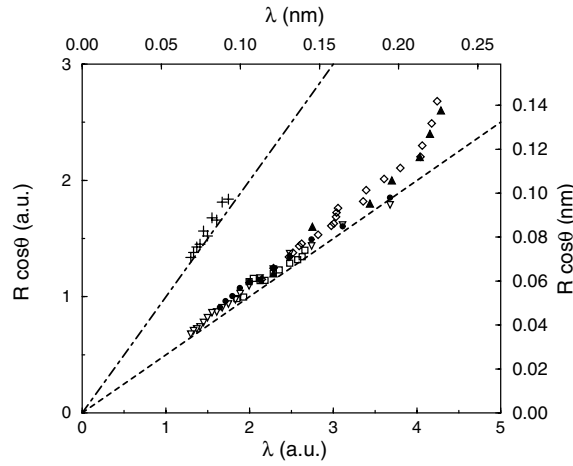


Figure 17. Projection of the internuclear distance on the polarization axis, $R \cos \theta$, versus the de Broglie wavelength of the recolliding electron for which the harmonic yield is minimal. The wavelength is calculated via the heuristic approach explained in the text. From [126]. Copyright (2002) by the American Physical Society.

equation (33). The relation between harmonic frequency and electron wavelength has sometimes been called ‘dispersion relation’ although in contrast to usual dispersion relations, frequency and wavelength belong to different objects here (photon/electron). For a discussion in the context of atomic HHG, see [137].

The 2D calculations for H_2^+ were followed by 3D calculations that led to the same findings: in [127], a 3D soft-core potential was employed in TDSE simulations on a numerical grid, while later, Lagmago Kamta and Bandrauk [129, 130] applied a basis-set expansion to the TDSE for the bare two-centre Coulomb potential of H_2^+ . Results of Lagmago Kamta and Bandrauk are shown in figure 18. The spectra on the left-hand side are the full harmonic spectra for H_2^+ , while the spectra on the right-hand side show the incoherent sum of the spectra from the two centres in H_2^+ , clearly showing the effect of the destructive interference between both centres.

A deeper analysis reveals that the two-point emitter model does not follow as naturally as it might seem from the two-centre nature of the molecule. The analytical derivation given in [126] holds only for short-range potentials and does not directly apply to real molecules. In any case, the interference interpretation implies that the observed minima are dictated by the recombination matrix element $\langle \Psi_c | \hat{O} | \Psi_0 \rangle$ where Ψ_0 is the initial state of the electron, Ψ_c is the continuum state with the electron energy that corresponds to a given harmonic frequency, and \hat{O} is the transition operator which is, depending on the theoretical model, either the dipole, the dipole momentum, or the dipole acceleration operator. Three ingredients are needed to arrive at simple two-centre interference formulae: (i) the plane-wave approximation for the continuum states, i.e. $\Psi_c \sim \exp(i\mathbf{k}r)$, (ii) usage of the dipole *momentum* operator and (iii) the initial state in the form of a linear combination of atomic orbitals (LCAO), i.e. $\Psi_0(\mathbf{r}) \sim \varphi_0(\mathbf{r} - \mathbf{R}/2) + \varphi_0(\mathbf{r} + \mathbf{R}/2)$. In this case, we obtain

$$\langle \Psi_c | \hat{O} | \Psi_0 \rangle \sim 2 \cos(\mathbf{k} \cdot \mathbf{R}/2) \langle \exp(i\mathbf{k} \cdot \mathbf{r}) | \hat{O} | \varphi_0 \rangle, \quad (34)$$

where the interference is explicitly expressed by the cosine function, leading to equations (31), (32). In [130], where only dipole and acceleration forms were considered, it was shown that the two-point emitter formulae follow from the acceleration form, if large

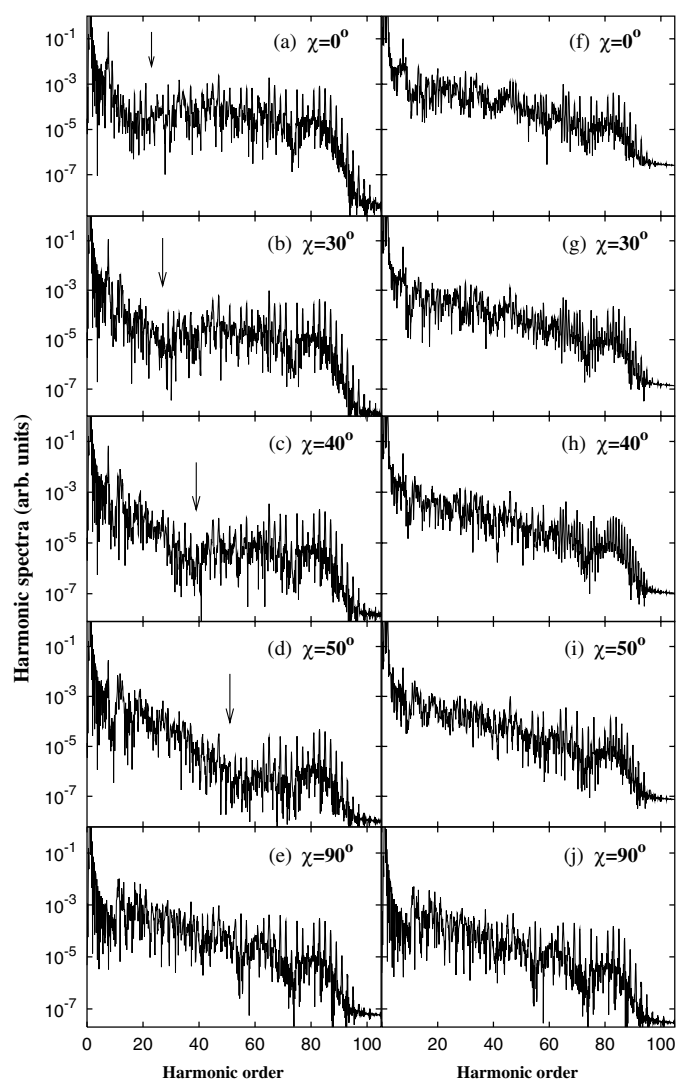


Figure 18. Harmonic spectra for H_2^+ at $R = 2$ au, aligned at various angles χ , in an 800 nm laser pulse with intensity $5 \times 10^{14} \text{ W cm}^{-2}$. Left: full spectra; right: incoherent sum of spectra from the two centres. Reprinted with permission from [130]. Copyright (2005) by the American Physical Society.

internuclear distance is assumed as an additional approximation. A similar discussion can be found in [119].

The simple two-centre interference picture breaks down when the initial electron orbital cannot be approximated by a simple LCAO wavefunction with only one atomic orbital per site. In [138], HHG from N_2 molecules was investigated with the result that the minima and maxima cannot be understood within the two-point emitter model. This is due to the fact that the HOMO of N_2 has substantial contributions from both atomic s- and p-orbitals. Note that the calculation of [138] restricts itself to the evaluation of the recombination amplitude, but it is based on *ab initio* molecular orbitals as well as accurate continuum states *beyond* the plane-wave approximation.

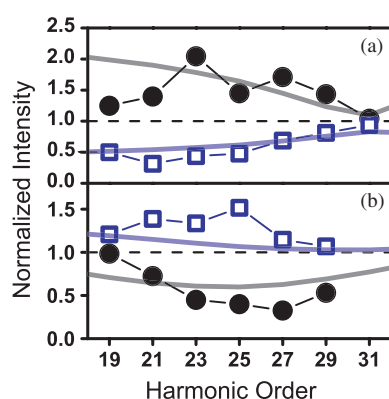


Figure 19. Harmonics in aligned N₂ (a) and CO₂ (b) molecules, divided by the yield of harmonics in a randomly aligned sample. The filled (open) symbols show the measurement for molecules aligned such that ionization is enhanced (suppressed). The black and blue curves show results of calculations for the two cases. Reprinted with permission from [131]. Copyright (2005) by the Nature Publishing Group.

A good candidate for the study of two-centre interference is the CO₂ molecule. Although it is triatomic (linear structure OCO), its π_g doubly degenerate HOMO is very similar to that of O₂ with two nodal planes, one along the molecular axis and one perpendicular to the molecular axis. It looks similar to two atomic p-orbitals centred at each O atom and can thus be approximated by an LCAO wavefunction with one atomic orbital per site. The distance between the O atoms (4.4 au) is larger than the bondlength of the common diatomic molecules, so that the two centres are well separated, and the conditions for the observation of the interference effect are favourable. In fact, the experimental demonstration of destructive intramolecular interference in HHG was achieved with aligned CO₂ molecules [131, 132]. An important difference with respect to H₂⁺ and H₂ is that the two atomic orbitals are added with opposite signs. This leads to an interchange of interference minima and maxima [126]. To prove that the observed suppression of HHG in CO₂ aligned parallel to the laser field was indeed due to destructive interference rather than related to the ionization step in the three-step model, Kanai *et al* [131] measured simultaneously the ionization yield. They aligned different molecular species using the impulsive alignment technique [43, 44], where the molecules are ‘kicked’ by a short pulse and become aligned at certain revival times after the alignment pulse is over. Harmonics are generated by employing a second laser pulse at times when the molecules are aligned, and the ion signal is measured at the same time. Figure 19 shows the harmonics for N₂ (panel (a)) and CO₂ molecules (panel (b)), normalized to the harmonics in a randomly aligned sample. Harmonics are generated at times when the ionization yield is enhanced (filled circles) or suppressed (open squares) due to alignment. In N₂, HHG is enhanced together with ionization, while in CO₂ the behaviour is opposite: HHG is suppressed when ionization is enhanced and vice versa. This means that the minimum of HHG in CO₂ cannot come from the ionization step, but must originate from recombination interference. The position of the minimum in the normalized spectrum is found at the 27th harmonic, see figure 19(b). Vozzi *et al* [132] measured over a wider range of harmonic orders and found the minimum for CO₂ at the 33rd harmonic, see figure 20. This raises an interesting detail, namely the question which relation between harmonic frequency and electron wavelength determines the interference accurately. It was argued by Vozzi *et al* that the Coulomb correction in equation (33) (see discussion above) should not be made for CO₂. A possible explanation is

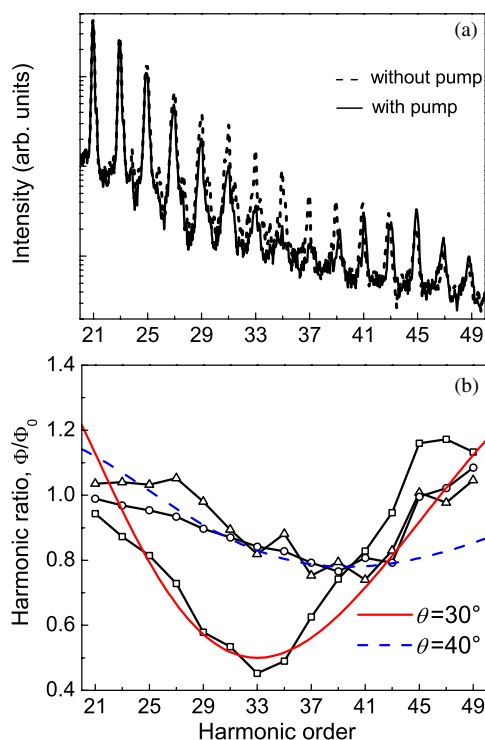


Figure 20. (a) Harmonic spectra from CO_2 molecules with and without aligning pulse. The delay time of 21.1 ps between aligning pulse and driving pulse corresponds to a dominating angle of alignment of $\theta \approx 30^\circ$. (b) Ratio of spectra with and without aligning pulse for the three different delay times 20.7 ps (circles), 21.1 ps (squares) and 21.3 ps (triangles) between aligning pulse and probe pulse generating the harmonics. Solid and dashed curves: prediction of the two-centre interference model for $\theta = 30^\circ$ and $\theta = 40^\circ$. Reprinted with permission from [132]. Copyright (2005) by the American Physical Society.

that the O–O distance in CO_2 is much larger than the bondlengths of H_2 and H_2^+ so that the distortion of the electron wave due to the core potential might be less relevant.

Recently, Kanai *et al* have measured the ellipticity dependence of HHG for aligned molecules [139]. They found that for N_2 aligned parallel to the laser field, the 31st harmonic is suppressed in a small range around zero ellipticity, in contrast to HHG from atoms. Although the simple two-point emitter model cannot be applied to N_2 , Kanai *et al* argue that the suppression is a signature of (more complicated) destructive interference.

We conclude that the two-centre interference in HHG can be used to determine the internuclear distance in a sample of aligned molecules. It could be a powerful tool to directly probe the nuclear positions in a molecule on ultrafast time scales. However, as a method it seems to require that the initial electron orbital is of the LCAO form. Otherwise it is not obvious how to read the interference pattern.

A more general approach to retrieve the information about the molecule from HHG spectra is the *molecular-orbital tomography* proposed by Itatani *et al* [1]: if the HHG spectra and phases are known for the whole range of molecular orientations, then a tomographic algorithm can be applied so that a 2D projection of the initial electron orbital Ψ_0 is reconstructed. The principle is analogous to computer tomography of a human being: 2D images taken from all sides allow the reconstruction of the full 3D structure. Molecular tomography rests on the

fact that HHG is very sensitive to the recombination matrix element, which in the plane-wave approximation for the continuum electron becomes a Fourier transform,

$$\mathbf{d}(\omega) = \langle \exp(i\mathbf{k} \cdot \mathbf{r}) | \hat{O} | \Psi_0 \rangle. \quad (35)$$

The crucial prerequisite for tomography is that the direction of \mathbf{k} is fixed. This is usually well satisfied in HHG because the electron is driven mainly along the laser polarization axis. The absolute value of \mathbf{k} is determined by the frequency ω of the harmonic under consideration, see the discussion of the ‘dispersion relation’ above. Equation (35) can be viewed as a 1D Fourier transform along the polarization axis applied to the orbital Ψ_0 , integrated along the directions perpendicular to \mathbf{k} , or equivalently as a 1D cut through the 3D Fourier transform of Ψ_0 . Consequently, if this quantity is known for all possible orientations of the molecule, one knows the full 3D Fourier transform. In principle, the orbital Ψ_0 is then retrieved by the inverse Fourier transformation. (The procedure is slightly complicated by the presence of the transition operator [1].)

The question remains how the recombination matrix element (35) is obtained from the measured harmonic amplitude. In Itatani *et al* [1], the dipole form of the recombination matrix element is used and the harmonic intensity is written as

$$S(\omega, \theta) \sim \omega^4 |a(\omega) \mathbf{d}(\omega, \theta)|^2, \quad (36)$$

i.e. all information besides the matrix element \mathbf{d} is basically collected in the factor $a(\omega)$ which is taken to be independent of the orientation θ except for a prefactor proportional to the ionization probability. This assumption is well justified at least for the N_2 molecule studied in [1]. From a measurement of the harmonic spectrum for a reference atom with known orbital (i.e. known recombination matrix element), $a(\omega)$ can be obtained. This information is then used in order to deduce the molecular $\mathbf{d}(\omega)$ from the measured HHG spectra at various orientations. The phase and direction of \mathbf{d} were set according to physical arguments in [1], but in principle even this information could be measured [24, 140, 141]. Having obtained $\mathbf{d}(\omega)$ for all angles, the tomographic reconstruction can be carried out¹.

The result of the experimental tomographic reconstruction of the N_2 orbital is shown in figure 21(a). Panel (b) shows an *ab initio* orbital for comparison, and the third panel compares cuts along the x -axis. Although the reconstruction is not perfect it gives a very good qualitative picture of the orbital, and it certainly reproduces the correct symmetry, orientation and nodal structure of the orbital.

Recently, it has been realized that the factorized form (36), which is essential for tomography, holds only when, either (i) the molecular orbital is symmetric or antisymmetric, or (ii) the laser pulse is very short so that any given harmonic is dominated by electrons recolliding from only one side of the molecule [142].

The discussion so far was based on the idea that HHG is dominated by only one single-electron orbital, and it was silently assumed that this is the HOMO. In fact, prior to the tomography work [1], all implementations of the Lewenstein models used the SAE approximation. Recently, however it became clear that multielectron systems such as the N_2 molecule require a deeper analysis. The dipole form of the recombination amplitude was investigated in [133, 135, 136] and it was found that in an n -electron system with the ground states of the neutral and the ionized system approximated by Slater determinants, two corrections arise in the recombination amplitude.

¹ Strictly speaking, two angles are needed to fix the orientation of the cylindrically symmetric N_2 orbital completely. In the experiment one varies only one angle, namely the angle θ between molecule and laser field. This limitation results in the tomographic reconstruction yielding a 2D object, namely the projection of the orbital onto a plane through the molecular axis.

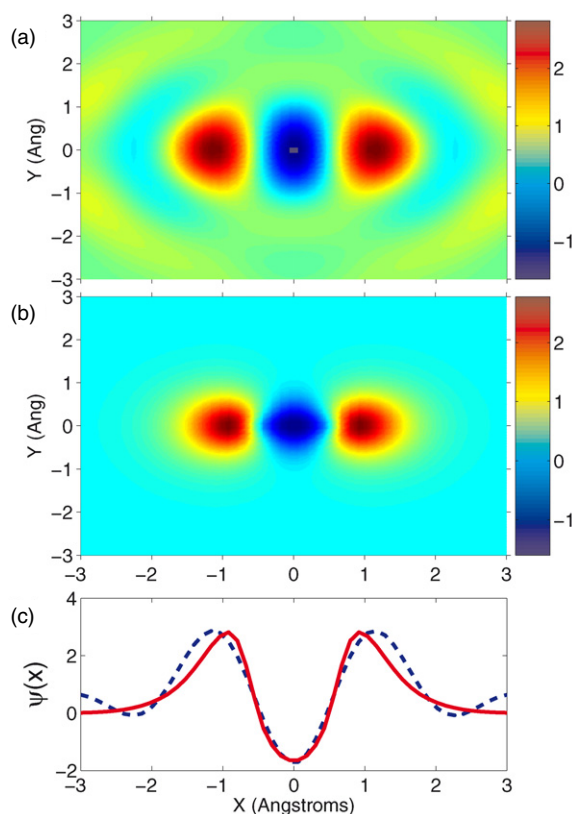


Figure 21. (a) Tomographic reconstruction based on measured harmonic spectra from aligned N_2 molecules; (b) *ab initio* N_2 orbital; (c) comparison of cuts along the x -axis. Reprinted with permission from [1]. Copyright (2004) by the Nature Publishing Group.

- (i) First, the HOMO should be replaced by the Dyson orbital φ_D , which can be regarded as the overlap between the ground states Ψ_0 , Ψ^+ of the neutral and ionized systems:

$$\varphi_D(\mathbf{r}) = \sqrt{n} \langle \Psi^+ | \Psi_0 \rangle. \quad (37)$$

Here, both states are assumed to be spatially nondegenerate. A singlet state and a degenerate doublet are assumed for the neutral molecule and the ion, respectively.

- (ii) Second, exchange terms appear in the dipole matrix element due to the indistinguishability of the electrons (see [133, 135, 136] for explicit expressions).

The Dyson orbital agrees with the Hartree–Fock HOMO up to second-order many-body perturbation theory. The exchange terms, however, appear already in lower order and are therefore normally more important. In practice, this means that the reconstruction of the HOMO requires some *a priori* knowledge about the bound orbitals. If the exchange corrections are sufficiently small, the reconstruction can still give a very good qualitative picture of the HOMO, see the example for N_2 in [135, 136].

A theoretical test of the orbital tomography is found in [143], where the Lewenstein model is used to calculate ‘experimental’ spectra. These are then used to reconstruct the HOMO. Note that these ‘experimental’ spectra involve the SAE as well as the plane-wave approximation. Nevertheless it is found that because of the limited frequency range of the

harmonic plateau, the reconstruction is still not perfect. It can be improved by extending the frequency range, for example by using a longer laser wavelength.

Orbital tomography has stimulated controversial discussions [144] since it came as a surprise to many scientists that one could measure the phase of a quantum mechanical electron orbital. Clearly, tomography in its present form is based on a model that quantifies HHG using a number of approximations, limiting the accuracy of the procedure. One of them is the usage of plane waves as continuum states. However, it is an accepted practice that every measurement in physics builds on a model that we assume to hold for the physical situation of interest. To give a provocative example, we would not normally use Heisenberg's uncertainty principle to rule out the possibility of measuring simultaneously the speed and position of a car. Rather, we assume that in this situation, classical physics is a model accurate enough for many purposes, e.g. for imposing a fine. Much in the same way, tomography measures an object (namely the HOMO, if multielectron corrections are neglected) that appears in the Lewenstein model, and we assume that the Lewenstein model is a good model of laser-matter interactions. The measured object, then, is useful and important not only for laser interactions but also for understanding other molecular properties such as chemical bonding.

5.3. Dynamical imaging

It is obvious that the ideas described so far can be utilized in a pump-probe scheme to measure the dynamics of a molecular process: a femtosecond pump pulse initiates a reaction, while a second strong pulse generates harmonics. Variation of the pump-probe delay time gives access to the time evolution. A demonstration that the HHG signal is sensitive to a chemical transition was given by Hay *et al* [145]. They dissociated I₂ molecules with 300 ps 789 nm laser pulses and found that the dissociation causes a strong increase in the HHG signal generated with a 70 fs 789 nm pulse.

Lately, Wagner *et al* [146] have used HHG in a femtosecond pump-probe experiment on SF₆ molecules with 25 fs 790 nm pulses. The pump pulse excites vibrations by Raman scattering. The harmonics generated by the probe pulse were measured as a function of the delay time. The temporal Fourier transform of the 39th harmonic showed clearly the vibrational frequencies of the excited modes in SF₆. This HHG-based method proved to be extremely sensitive: first, *all* excited modes could be observed in contrast to stimulated Raman scattering and second, clear modulations of the harmonics were found despite the very small estimated changes in the internuclear distances by only 2%.

Furthermore, we mention that for a sufficiently long pulse acting on vibrating molecules, satellite peaks are predicted to appear between the odd harmonics [147]. The spacing between the side peaks is given by the vibrational oscillation frequency.

With the conventional pump-probe approach described above, femtosecond temporal resolution is possible. However, it has been proposed and demonstrated that HHG can even pave the way for sub-fs measurements. Niiikura *et al* [148] have proposed the observation of bound-state electron dynamics. In their model calculation of laser-molecule interaction, the molecule is prepared in a superposition of electronic ground and excited states. They show that the harmonic spectrum exhibits a strong modulation which results from the sub-fs oscillation of the bound-state electron wave packet. By using one-to-one mapping between harmonic order and emission time (see section 2), they map the modulation in frequency to a modulation in time, giving an image of the bound-state motion.

A recent technique to measure proton dynamics on a sub-fs time scale is the PACER method (probing attosecond dynamics by chirp encoded recollision), theoretically proposed in [149] and experimentally demonstrated in [2]. It relies on one-to-one mapping between

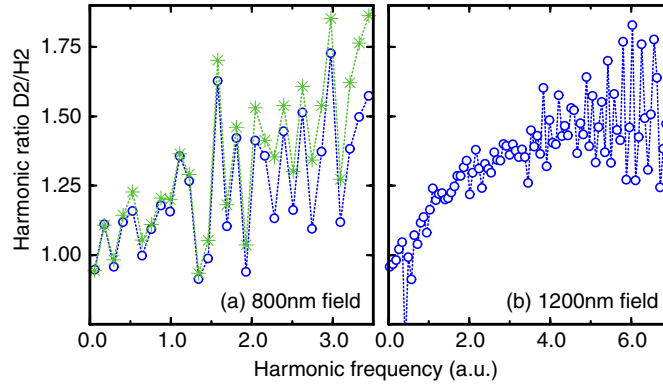


Figure 22. Calculated ratios between harmonic intensities in the isotopes D_2 and H_2 driven by a 780 nm or 1200 nm laser field with intensity $4 \times 10^{14} \text{ W cm}^{-2}$. Blue circles: molecules aligned perpendicular to the laser polarization. Green stars: random alignment. Data from [149].

harmonic frequency and the travel time of the electron. Each harmonic can be regarded as the probe signal in a pump-probe scheme with tunnel ionization as pump process and recollision as probe. The variation of the pump-probe delay time is simply achieved by observing various harmonic orders. The most practical way to isolate the effect of the nuclear dynamics is to take the ratio of harmonics generated in two different isotopes. The electron dynamics is the same in isotopes; differences in the spectrum are caused by the nuclear motion only.

The difference between isotopes was first seen in TDSE calculations for H_2 [149]. The Hamiltonian includes the vibration of the protons coupled to electron motion without Born–Oppenheimer approximation. The following simplifications are made: (i) fixed direction of the molecular axis, (ii) SAE approximation, (iii) two-dimensional motion of the active electron. The effective electron–core interaction is adjusted such that the model exactly reproduces the BO potentials of H_2 as well as H_2^+ when the system is ionized. The resulting ratio between harmonic spectra in the isotopes D_2 and H_2 is shown in figure 22. D_2 tends to generate more intense harmonics than H_2 , with the ratio increasing as a function of harmonic order. The molecules were chosen to be perpendicular to the laser field in order to suppress signatures of two-centre interference. The result for an ensemble of randomly aligned molecules, shown in figure 22(a), shows very similar behaviour. In order to understand the effect quantitatively, the Lewenstein model can be extended to include the vibrational motion [149, 150]. With the BO form of the H_2 ground state, $\Psi_0(\mathbf{r}, \mathbf{r}', R) = \chi_0(R)\psi_R(\mathbf{r}, \mathbf{r}')$, the dipole moment in the extended Lewenstein model reads

$$D(t) = -2\frac{i}{\hbar} \int_0^t dt' \left(\frac{2\pi m\hbar}{i(t-t') + \epsilon} \right)^{3/2} \int_0^\infty dR \chi_0^*(R) d_r^*(\mathbf{p}_s(t', t) + e\mathbf{A}(t)) \\ \times \exp\left(-\frac{iS(t', t)}{\hbar}\right) \hat{U}_R(t-t') d_i(\mathbf{p}_s(t', t) + e\mathbf{A}(t'), t') \chi_0(R) + \text{c.c.} \quad (38)$$

This equation corrects equation (3) of [150] which contained typographical errors. The saddle-point approximation for the integration over momenta has been made, giving rise to the appearance of the saddle-point momentum

$$\mathbf{p}_s(t', t) = -e \int_{t'}^t \mathbf{A}(t'')/(t-t'') dt'' \quad (39)$$

The prefactor of 2 in equation (38) is due to the presence of two electrons that can become active. Exchange terms as discussed in the context of orbital tomography are ignored in

this spatially symmetric two-electron system since they vanish for symmetry reasons, as long as a single-particle orbital description without correlation is considered. Equation (38) is formally very similar to equation (26) except for the appearance of the time-evolution operator $\hat{U}_R(t-t')$ that propagates the vibrational wave packet in the BO potential of the molecular ion. Furthermore, the matrix elements d_i and d_r depend on the internuclear distance R ,

$$d_i(\mathbf{p}, t) = \langle \psi_{\text{PW}}(\mathbf{p}) \psi_R^+ | eE(t)z | \psi_R \rangle_{rr'}, \quad (40)$$

$$d_r(\mathbf{p}) = \langle \psi_{\text{PW}}(\mathbf{p}) \psi_R^+ | -e\mathbf{r} | \psi_R \rangle_{rr'}, \quad (41)$$

with $\psi_R^+(r')$ being the electronic ground-state wavefunction of H_2^+ . If the dependence on R is neglected as suggested in [149] (which amounts to neglecting the two-centre interference), a simplified expression for the dipole moment arises. It is the same as the atomic expression except for the additional appearance of the vibrational autocorrelation function

$$C(\tau) = \int_0^\infty dR \chi^*(R, 0) \chi(R, \tau) \quad (42)$$

in the SFA integral. Here $\chi(R, \tau)$ is the time-dependent vibrational wave packet with $\tau = 0$ being the time of ionization. This shows that heavier isotopes generate harmonics more efficiently, because slower nuclear motion makes the autocorrelation function deviate less from unity. The difference between isotopes will be more pronounced for longer travel times τ . Via the one-to-one mapping between travel times and harmonic frequencies, this means that the ratio D_2/H_2 increases with harmonic order in agreement with figure 22.

If the dependence of the recombination matrix element on the internuclear distance is taken into account, the simple picture based on the autocorrelation function (42) breaks down. Nevertheless, if the Lewenstein model in the momentum form is considered in combination with the LCAO approximation for the electronic ground states of H_2 and H_2^+ , one can show that the recombination matrix element is proportional to $\cos(\mathbf{p} \cdot \mathbf{R}/2)$, with \mathbf{p} being the momentum of the recolliding electron. If other dependences on the molecular orientation are neglected, integration over all orientations leads to the ‘interference kernel’ $f(p, R) = \sin(pR/2)/(pR/2)$ and the autocorrelation function is replaced by the correlation function

$$C(\tau, p) = \int_0^\infty dR \chi^*(R, 0) f(p, R) \chi(R, \tau) \quad (43)$$

in the SFA integral.

The difference between HHG in D_2 and H_2 was confirmed in the experiment by Baker *et al* [2], see figure 23 for the raw data of the measured harmonics. For quantitative analysis, the ratio was taken, see figure 24. The experimental ratio agrees well with the theoretical curve obtained as the modulus squared of the ratio of correlation functions for vibrational motion in D_2^+ and H_2^+ , see equation (43). We can reconstruct the nuclear motion from the measured ratio by applying an iterative scheme using a genetic algorithm [2, 149]. The algorithm searches for a BO potential that is optimal in the sense that it leads to vibrational motion with a correlation function ratio close to the measured ratio of harmonics. Although the iteration does not converge to a unique solution, the results of different runs do not differ much from each other. The red curves in figure 25 show the internuclear distance as a function of time obtained from various runs. The axes of this graph show that a measurement of proton and deuteron dynamics has been carried out with a spatial resolution finer than one Bohr radius and with sub-fs temporal resolution. If one regards the separation between two harmonic peaks as the factor determining the time resolution, one estimates 100 attoseconds.

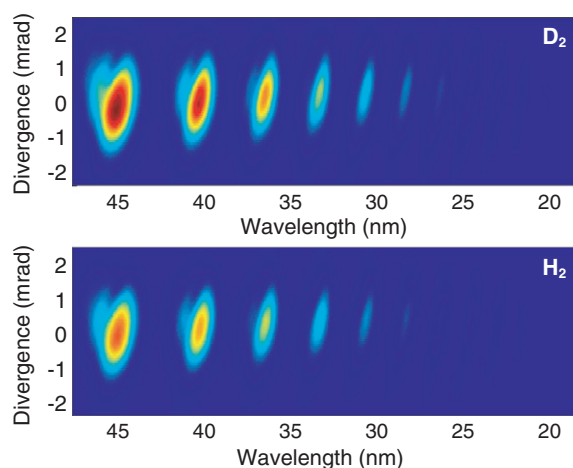


Figure 23. CCD images of harmonics from D_2 and H_2 molecules in 8 fs 775 nm pulses with intensity $2 \times 10^{14} \text{ W cm}^{-2}$. D_2 generates harmonics more efficiently. Reprinted from [2].

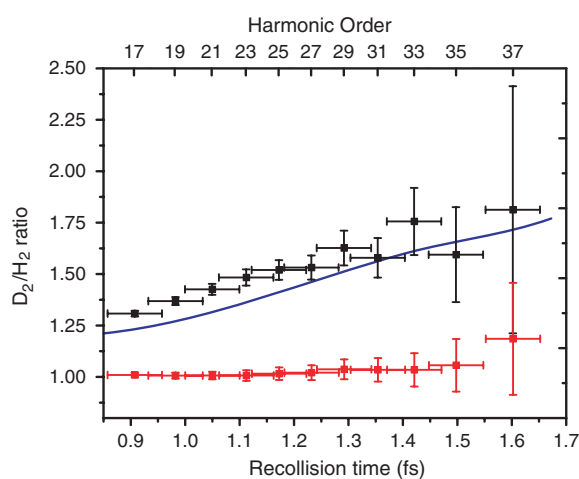


Figure 24. Ratio of harmonic peak intensities for D_2 and H_2 at equal density (black points, upper data set). Control ratio of two harmonic spectra for H_2 (red points, lower data set). The theoretical prediction for the ratio D_2/H_2 based on the correlation function (43) including two-centre interference is shown as the blue curve. Reprinted from [2].

In the modelling of the experiment, random alignment has been assumed. In this case, the influence of two-centre interference on the ratio D_2/H_2 , although present, is small. Interference becomes pronounced when aligned molecules are considered. Figure 26 shows the ratios obtained from the full evaluation of the momentum-form SFA for a few fixed molecular orientations. The solid line is from a simplified model based on the correlation function (43). This model is slightly different from the simple correlation function ratio used in the modelling of the experiment, see [150] for details. Again, the ratio generally increases with harmonic order, but at sufficiently small orientation angles θ , we observe an additional feature in the ratio: a modulation consisting of a maximum and a minimum related to destructive interference in H_2 and D_2 respectively. Similar to the interference dip in the spectra shown

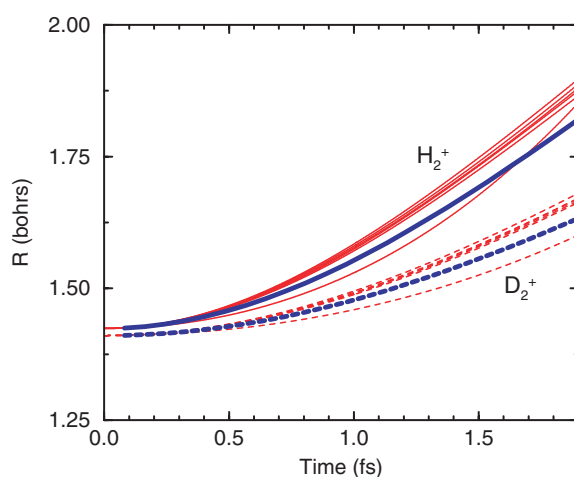


Figure 25. Expectation value of the internuclear distance as a function of time after ionization of H_2 (solid curves) or D_2 (dashed curves). The thin red curves represent the reconstruction from the experimental data obtained from different runs of the iterative algorithm. The thick blue curves result from vibrational dynamics calculated with the exact BO potential. Reprinted from [2].

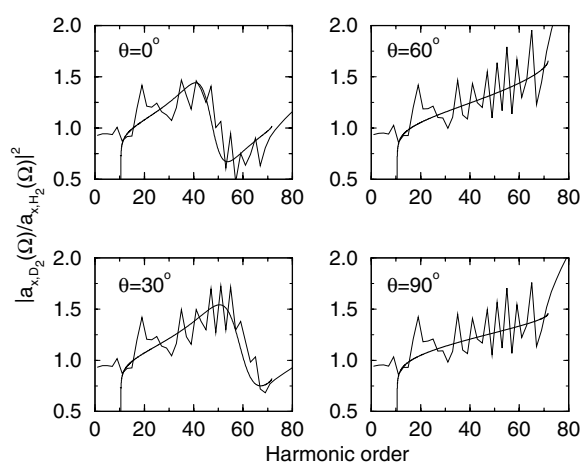


Figure 26. SFA calculations of the ratio of harmonics in D_2 and H_2 for various orientations of the molecular axis. The laser field has 800 nm wavelength and $5 \times 10^{14} \text{ W cm}^{-2}$ intensity. Reprinted from [150].

in figures 14, 15 and 18, the interference modulation shifts to higher orders with increasing orientation angle.

Interference and dynamical effects both influence the harmonics. This gives exciting perspectives on dynamical imaging of structure. At the same time, it is a major challenge for theoretical modelling. In [2], not only harmonics from H_2 and D_2 , but also from CH_4 and CD_4 have been compared. Again, the signature of sub-fs dynamics could be clearly observed, indicating ultrafast rearrangement of the CH_4^+ geometry immediately after ionization, but an extension of the theory to multi-atom molecules is needed to interpret the data quantitatively.

6. Conclusion

Molecular imaging via electron recollision is highly attractive because it combines the ideas from conventional imaging techniques, such as diffraction, with the ultrafast time scale of femtosecond pulses. Moreover, using the schemes that we have discussed in sections 4 and 5, the recollision dynamics can be exploited such that measurements with attosecond resolution become possible. The science discussed in this review therefore overlaps to some extent with attosecond science. It is important to realize, however, that we use laser-induced electron dynamics in molecules as a diagnostic tool rather than as a technology to build XUV light sources. By using directly the sub-cycle duration of recolliding electron wave packets, we circumvent the need for attosecond pulses for attosecond measurements. A limitation of the sub-cycle schemes, where ionization acts as the pump step and recollision acts as probe step, is that the evolution of the system necessarily takes place in the presence of a strong field. Positively viewed, however, this provides us with an elegant tool to study the dynamics of field-dressed states.

We have made a classification into three categories: diffraction-based, fragmentation-based and HHG-based methods. In all cases, the returning electron probes the molecule, but the observables are different: electrons, ions or high harmonics, respectively. Experimental realizations have been demonstrated for the second and third categories. In simple terms, diffraction and fragmentation take a snapshot of the nuclear positions at the time of recollision, while harmonics are sensitive to the initial electronic state of the molecule, creating the possibility to image orbitals. This has been systematically exploited in the orbital tomography scheme. In a few words, the present experimental status of the field can be summarized as follows: (i) the positions of nuclei in the simplest molecular systems H_2^+ , D_2^+ have been traced on the sub-femtosecond time scale, (ii) the static structure of electronic orbitals and nuclear positions in small molecules have been imaged.

Although the idea of recollision imaging has been present for more than a decade, it has received a strong boost in the last few years by the combination of molecular alignment with high-harmonic generation. Molecular imaging via harmonic generation and controlling harmonics by molecular manipulation are two sides of the same coin. The alignment of polyatomic molecules [151] and the orientation of polar molecules [152] will provide new targets of investigation.

For several reasons it can be anticipated that the dynamics of bound electronic wave packets as well as the coupling between bound electronic states will be very important for future work. With the advent of strong infrared (1–3 μm) laser pulses, ionized H_2 molecules will have more time to evolve in the time between ionization and recombination, giving rise to laser-induced coupling between ground state and first excited state. Ionization of more complex molecules does not necessarily populate only one electronic state of the ion. For example, the lowest states of the methane ion lie close together and exhibit Jahn–Teller coupling [153]. Independent of these specific examples, the observation of bound-state electron wave packets, e.g. following fast removal of an electron [154], is the natural domain of attosecond science and will therefore play a central role also in recollision imaging.

Acknowledgments

The author wishes to express his gratitude for useful discussions with C Chirilă, P Corkum, C D Lin, J Marangos, D Villeneuve and E van der Zwan, and for discussions within the NSERC SRO network ‘Controlled electron re-scattering: femtosecond, sub-angstrom imaging of single molecules’.

References

- [1] Itatani J *et al* 2004 *Nature* **432** 867
see also Stapelfeldt H 2004 *Nature* **432** 809
- [2] Baker S *et al* 2006 *Science* **312** 424
- [3] Robinson I K and Tweet D J 1992 *Rep. Prog. Phys.* **55** 599
- [4] Rischel C *et al* 1997 *Nature* **390** 490
- [5] Ihee H *et al* 2001 *Science* **291** 458
- [6] Zewail A H 2000 *J. Phys. Chem. A* **104** 5660
- [7] Kienberger R *et al* 2004 *Nature* **427** 817
- [8] Assion A *et al* 1998 *Science* **282** 919
- [9] Wollenhaupt M, Engel V and Baumert T 2005 *Ann. Rev. Phys. Chem.* **56** 25
- [10] Paulus G G *et al* 1994 *Phys. Rev. Lett.* **72** 2851
- [11] Niikura H *et al* 2002 *Nature* **417** 917
- [12] Fittinghoff D N, Bolton P R, Chang B and Kulander K C 1992 *Phys. Rev. Lett.* **69** 2642
- [13] Walker B *et al* 1994 *Phys. Rev. Lett.* **73** 1227
- [14] Becker A and Faisal F H M 2000 *Phys. Rev. Lett.* **84** 3546
- [15] Lein M, Gross E K U and Engel V 2000 *Phys. Rev. Lett.* **85** 4707
- [16] Bhardwaj V R, Rayner D M, Villeneuve D M and Corkum P B 2001 *Phys. Rev. Lett.* **87** 253003
- [17] Staudte A *et al* 2002 *Phys. Rev. A* **65** 020703
- [18] Sakai H, Larsen J J, Wendt-Larsen I, Olesen J and Corkum P B 2003 *Phys. Rev. A* **67** 063404
- [19] Rudenko A, Feuerstein B, Zrost K, de Jesus V L B, Ergler T, Dimopoulou C, Schröter C D, Moshhammer R and Ullrich J 2005 *J. Phys. B: At. Mol. Opt. Phys.* **38** 487
- [20] Baier S, Ruiz C, Plaja L and Becker A 2006 *Phys. Rev. A* **74** 033405
- [21] McPherson A *et al* 1987 *J. Opt. Soc. Am. B* **4** 595
- [22] L'Huillier A, Schafer K J and Kulander K C 1991 *J. Phys. B* **24** 3315
- [23] Paul P M, Toma E S, Breger P, Mullot G, Augé F, Balcou P, Muller H G and Agostini P 2001 *Science* **292** 1689
- [24] Mairesse Y *et al* 2003 *Science* **302** 1540
- [25] Tzallas P, Charalambidis D, Papadogiannis N A, Witte K and Tsakiris G D 2003 *Nature* **426** 267
- [26] Drescher M, Hentschel M, Kienberger R, Tempea G, Spielmann C, Reider G A, Corkum P B and Krausz F 2001 *Science* **291** 1923
- [27] Hentschel M *et al* 2001 *Nature* **414** 509
- [28] Agostini P and DiMauro L F 2004 *Rep. Prog. Phys.* **67** 813
- [29] Scrinzi A, Ivanov M Y, Kienberger R and Villeneuve D M 2006 *J. Phys. B: At. Mol. Opt. Phys.* **39** R1
- [30] Niikura H and Corkum P B 2007 *Adv. At. Mol. Opt. Phys.* **54** 511
- [31] Nisoli *et al* 1997 *Opt. Lett.* **22** 522
- [32] Morgner U *et al* 1999 *Opt. Lett.* **24** 411
- [33] Steinmeyer G, Sutter D H, Gallmann L, Matuschek N and Keller U 1999 *Science* **286** 1507
- [34] <http://www.allis.ca>
- [35] Kitzler M and Lezius M 2005 *Phys. Rev. Lett.* **95** 253001
- [36] Alnaser A S *et al* 2005 *Phys. Rev. A* **72** 030702
- [37] Légaré F, Lee K F, Bandrauk A D, Villeneuve D M and Corkum P B 2006 *J. Phys. B: At. Mol. Opt. Phys.* **39** S503
- [38] Ergler T, Rudenko A, Feuerstein B, Zrost K, Schröter C D, Moshhammer R and Ullrich J 2006 *Phys. Rev. Lett.* **97** 193001
- [39] Friedrich B and Herschbach D R 1995 *Phys. Rev. Lett.* **74** 4623
- [40] Seideman T 1995 *J. Chem. Phys.* **103** 7887
- [41] Sakai H, Safvan C P, Larsen J J, Hilligsoe K M, Hald K and Stapelfeldt H 1999 *J. Chem. Phys.* **110** 10235
- [42] Larsen J J, Sakai H, Safvan C P, Wendt-Larsen I and Stapelfeldt H 1999 *J. Chem. Phys.* **111** 7774
- [43] Rosca-Pruna F and Vrakking M J J 2001 *Phys. Rev. Lett.* **87** 153902
- [44] Dooley P W, Litvinyuk I V, Lee K F, Rayner D M, Spanner M, Villeneuve D M and Corkum P B 2003 *Phys. Rev. A* **68** 023406
- [45] Torres R, de Nalda R and Marangos J P 2005 *Phys. Rev. A* **72** 023420
- [46] Leibscher M, Averbukh I S and Rabitz H 2003 *Phys. Rev. Lett.* **90** 213001
- [47] Stapelfeldt H and Seideman T 2003 *Rev. Mod. Phys.* **75** 543
- [48] Scrinzi A, Geissler M and Brabec T 1999 *Phys. Rev. Lett.* **83** 706
- [49] Milošević D B, Paulus G G, Bauer D and Becker W 2006 *J. Phys. B: At. Mol. Opt. Phys.* **39** R203
- [50] Corkum P B 1993 *Phys. Rev. Lett.* **71** 1994

- [51] Lewenstein M, Balcou P, Ivanov M Y, L'Huillier A and Corkum P B 1994 *Phys. Rev. A* **49** 2117
- [52] Salières P, L'Huillier A and Lewenstein M 1995 *Phys. Rev. Lett.* **74** 3776
- [53] Antoine P, L'Huillier A and Lewenstein M 1996 *Phys. Rev. Lett.* **77** 1234
- [54] Balcou P, Salières P, L'Huillier A and Lewenstein M 1997 *Phys. Rev. A* **55** 3204
- [55] Paulus G G, Becker W, Nicklich W and Walther H 1994 *J. Phys. B: At. Mol. Opt. Phys.* **27** L703
- [56] Paulus G G, Becker W and Walther H 1995 *Phys. Rev. A* **52** 4043
- [57] Brabec T, Ivanov M Y and Corkum P B 1996 *Phys. Rev. A* **54** R2551
- [58] Lein M 2003 *J. Phys. B: At. Mol. Opt. Phys.* **36** L155
- [59] Fischer R, Lein M and Keitel C H 2006 *Phys. Rev. Lett.* **97** 143901
- [60] de Nalda R, Heesel E, Lein M, Hay N, Velotta R, Springate E, Castillejo M and Marangos J P 2004 *Phys. Rev. A* **69** 031804
- [61] Zhou X X, Tong X M, Zhao Z X and Lin C D 2005 *Phys. Rev. A* **71** 061801
- [62] Zhou X X, Tong X M, Zhao Z X and Lin C D 2005 *Phys. Rev. A* **72** 033412
- [63] Madsen C B and Madsen L B 2006 *Phys. Rev. A* **74** 023403
- [64] Itatani J, Zeidler D, Levesque J, Spanner M, Villeneuve D M and Corkum P B 2005 *Phys. Rev. Lett.* **94** 123902
- [65] Shan B, Ghimire S and Chang Z 2004 *Phys. Rev. A* **69** 021404
- [66] Torres R *et al* 2007 *Phys. Rev. Lett.* **98** 203007
- [67] Lagmago Kamta G and Bandrauk A D 2006 *Phys. Rev. A* **74** 033415
- [68] Smyth E S, Parker J S and Taylor K T 1998 *Comput. Phys. Commun.* **114** 1
- [69] Parker J S, Moore L R, Dundas D and Taylor K T 2000 *J. Phys. B: At. Mol. Opt. Phys.* **33** L691
- [70] Keldysh L V 1965 *Sov. Phys.—JETP* **20** 1307
- [71] Becker A and Faisal F H M 2005 *J. Phys. B: At. Mol. Opt. Phys.* **38** R1
- [72] Reiss H R 1980 *Phys. Rev. A* **22** 1786
- [73] Ben-Tal N, Moiseyev N, Kosloff R and Cerjan C 1993 *J. Phys. B: At. Mol. Opt. Phys.* **26** 1445
- [74] Chu S-I and Telnov D A 2004 *Phys. Rep.* **390** 1
- [75] Tong X M, Zhao Z X and Lin C D 2002 *Phys. Rev. A* **66** 033402
- [76] Tong X M, Zhao Z X and Lin C D 2003 *Phys. Rev. Lett.* **91** 233203
- [77] Tong X M, Zhao Z X and Lin C D 2003 *Phys. Rev. A* **68** 043412
- [78] Moreno P, Plaja L and Roso L 1997 *Phys. Rev. A* **55** R1593
- [79] Bandrauk A D, Chelkowski S, Yu H and Constant E 1997 *Phys. Rev. A* **56** R2537
- [80] Kopold R, Becker W and Kleber M 1998 *Phys. Rev. A* **58** 4022
- [81] Chirilă C C and Lein M 2006 *Phys. Rev. A* **73** 023410
- [82] Lein M and Rost J M 2003 *Phys. Rev. Lett.* **91** 243901
- [83] Lein M 2005 *Phys. Rev. A* **72** 053816
- [84] Chirilă C C and Lein M 2006 *Phys. Rev. A* **74** 051401
- [85] Zuo T, Bandrauk A D and Corkum P B 1996 *Chem. Phys. Lett.* **259** 313
- [86] Muth-Böhm J, Becker A and Faisal F H M 2000 *Phys. Rev. Lett.* **85** 2280
- [87] Grasbon F *et al* 2001 *Phys. Rev. A* **63** 041402
- [88] Corkum P B private communication
- [89] Lein M, Marangos J P and Knight P L 2002 *Phys. Rev. A* **66** 051404
- [90] Spanner M, Smirmova O, Corkum P B and Ivanov M Y 2004 *J. Phys. B: At. Mol. Opt. Phys.* **37** L243
- [91] Yurchenko S N, Patchkovskii S, Litvinyuk I V, Corkum P B and Yudin G L 2004 *Phys. Rev. Lett.* **93** 223003
- [92] Hu S X and Collins L A 2005 *Phys. Rev. Lett.* **94** 073004
- [93] Heather R and Metiu H 1987 *J. Chem. Phys.* **86** 5009
- [94] Grobe R, Haan S L and Eberly J H 1999 *Comput. Phys. Commun.* **117** 200
- [95] Chelkowski S, Foisy C and Bandrauk A D 1998 *Phys. Rev. A* **57** 1176
- [96] Vager Z, Naaman R and Kanter E P 1989 *Science* **244** 426
- [97] Chelkowski S, Corkum P B and Bandrauk A D 1999 *Phys. Rev. Lett.* **82** 3416
- [98] Niikura H *et al* 2003 *Nature* **421** 826
- [99] Alnaser A S *et al* 2003 *Phys. Rev. Lett.* **91** 163002
- [100] Alnaser A S *et al* 2004 *Phys. Rev. Lett.* **93** 183202
- [101] Feuerstein B *et al* 2001 *Phys. Rev. Lett.* **87** 043003
- [102] de Jesus V L B, Feuerstein B, Zrost K, Fischer D, Rudenko A, Afaneh F, Schröter C D, Moshhammer R and Ullrich J 2004 *J. Phys. B: At. Mol. Opt. Phys.* **37** L161
- [103] Urbain X *et al* 2004 *Phys. Rev. Lett.* **92** 163004
- [104] Légraré F *et al* 2003 *Phys. Rev. Lett.* **91** 093002
- [105] Tong X M and Lin C D 2004 *Phys. Rev. A* **70** 023406
- [106] Seideman T, Ivanov M Y and Corkum P B 1995 *Phys. Rev. Lett.* **75** 2819

- [107] Zuo T and Bandrauk A D 1995 *Phys. Rev. A* **52** R2511
- [108] Delone N B and Krainov V P 1991 *J. Opt. Soc. Am. B* **8** 1207
- [109] Hu J, Han K-L and He G-Z 2005 *Phys. Rev. Lett.* **95** 123001
- [110] Hu J, Wang M-S, Han K-L and He G-Z 2006 *Phys. Rev. A* **74** 063417
- [111] Tong X M, Zhao Z X and Lin C D 2006 *Phys. Rev. Lett.* **97** 049301 (Comment)
Hu J, Han K-L and He G-Z 2006 *Phys. Rev. Lett.* **97** 049302 (Reply)
- [112] Schinke R 1993 *Photodissociation Dynamics* (Cambridge, UK: Cambridge University Press)
- [113] Yudin G L and Ivanov M Y 2001 *Phys. Rev. A* **63** 033404
- [114] Yudin G L and Ivanov M Y 2001 *Phys. Rev. A* **64** 035401
- [115] Sundaram B and Milonni P W 1990 *Phys. Rev. A* **41** 6571
- [116] Eberly J H and Fedorov M V 1992 *Phys. Rev. A* **45** 4706
- [117] Burnett K, Reed V C, Cooper J and Knight P L 1992 *Phys. Rev. A* **45** 3347
- [118] Lappas D G, Fedorov M V and Eberly J H 1993 *Phys. Rev. A* **47** 1327
- [119] Gordon A and Kärtner F X 2005 *Phys. Rev. Lett.* **95** 223901
- [120] Chirilă C C and Lein M 2007 *J. Mod. Opt.* **54** 1039
- [121] Yu H and Bandrauk A D 1995 *J. Chem. Phys.* **102** 1257
- [122] Lappas D G and Marangos J P 2000 *J. Phys. B: At. Mol. Opt. Phys.* **33** 4679
- [123] Velotta R, Hay N, Mason M B, Castillejo M and Marangos J P 2001 *Phys. Rev. Lett.* **87** 183901
- [124] Hay N, Velotta R, Lein M, de Nalda R, Heesel E, Castillejo M and Marangos J P 2002 *Phys. Rev. A* **65** 053805
- [125] Lein M, Hay N, Velotta R, Marangos J P and Knight P L 2002 *Phys. Rev. Lett.* **88** 183903
- [126] Lein M, Hay N, Velotta R, Marangos J P and Knight P L 2002 *Phys. Rev. A* **66** 023805
- [127] Lein M, Corso P P, Marangos J P and Knight P L 2003 *Phys. Rev. A* **67** 023819
- [128] Lein M, de Nalda R, Heesel E, Hay N, Springate E, Velotta R, Castillejo M, Knight P L and Marangos J P 2005 *J. Mod. Opt.* **52** 465
- [129] Lagmago Kamta G and Bandrauk A D 2004 *Phys. Rev. A* **70** 011404(R)
- [130] Lagmago Kamta G and Bandrauk A D 2005 *Phys. Rev. A* **71** 053407
- [131] Kanai T, Minemoto S and Sakai H 2005 *Nature* **435** 470
see also Marangos J P 2005 *Nature* **435** 435
- [132] Vozzi C *et al* 2005 *Phys. Rev. Lett.* **95** 153902
- [133] Santra R and Gordon A 2006 *Phys. Rev. Lett.* **96** 073906
- [134] Gordon A, Kärtner F X, Rohringer N and Santra R 2006 *Phys. Rev. Lett.* **96** 223902
- [135] Patchkovskii S, Zhao Z, Brabec T and Villeneuve D M 2006 *Phys. Rev. Lett.* **97** 123003
- [136] Patchkovskii S, Zhao Z, Brabec T and Villeneuve D M 2007 *J. Chem. Phys.* **126** 114306
- [137] Levesque J, Zeidler D, Marangos J P, Corkum P B and Villeneuve D M 2007 *Phys. Rev. Lett.* **98** 183903
- [138] Zimmermann B, Lein M and Rost J M 2005 *Phys. Rev. A* **71** 033401
- [139] Kanai T, Minemoto S and Sakai H 2007 *Phys. Rev. Lett.* **98** 053002
- [140] Wabnitz H *et al* 2006 *Eur. Phys. J. D* **40** 305
- [141] Kanai T, Takahashi E J, Nabekawa Y and Midorikawa K 2007 *Phys. Rev. Lett.* **98** 153904
- [142] van der Zwan E and Lein M submitted
- [143] Le V-H, Le A-T, Xie R-H and Lin C D 2007 *Preprint physics/0701250 v1* [physics.atom-ph]
- [144] Schwarz W H E 2006 *Angew. Chem. Int. Ed.* **45** 1508
- [145] Hay N, Velotta R, Mason M B, Castillejo M and Marangos J P 2002 *J. Phys. B: At. Mol. Opt. Phys.* **35** 1051
- [146] Wagner N L, Wüest A, Christov I P, Popmintchev T, Zhou X, Murnane M M and Kapteyn H C 2006 *Proc. Natl Acad. Sci. USA* **103** 13279
- [147] Corso P P, Fiordilino E and Persico F 2007 *J. Phys. B: At. Mol. Opt. Phys.* **40** 1383
- [148] Niikura H, Villeneuve D M and Corkum P B 2005 *Phys. Rev. Lett.* **94** 083003
- [149] Lein M 2005 *Phys. Rev. Lett.* **94** 053004
Chirilă C C and Lein M 2006 *J. Mod. Opt.* **53** 113
- [150] Chirilă C C and Lein M 2006 *J. Phys. B: At. Mol. Opt. Phys.* **39** S437
- [151] Lee K F, Villeneuve D M, Corkum P B, Stolow A and Underwood J G 2006 *Phys. Rev. Lett.* **97** 173001
- [152] Sakai H, Minemoto S, Nanjo H, Tanji H and Suzuki T 2003 *Phys. Rev. Lett.* **90** 083001
- [153] Vager Z, Kanter E P, Both G, Cooney P J, Faibis A, Koenig W, Zabransky B J and Zajfman D 1986 *Phys. Rev. Lett.* **57** 2793
- [154] Breidbach J and Cederbaum L S 2005 *Phys. Rev. Lett.* **94** 033901